

# Effective placement of self-centering damage-free connections for seismic-resilient steel moment resisting frames

Ludovica Pieroni<sup>1</sup>  | Fabio Freddi<sup>1</sup>  | Massimo Latour<sup>2</sup> 

<sup>1</sup> Department of Civil, Environmental & Geomatic Engineering, University College London, London, UK

<sup>2</sup> Department of Civil Engineering, University of Salerno, Salerno, Italy

## Correspondence

Ludovica Pieroni, Department of Civil, Environmental & Geomatic Engineering, University College London, London, UK  
Email: [ludovica.pieroni.20@ucl.ac.uk](mailto:ludovica.pieroni.20@ucl.ac.uk)

## Abstract

In recent years, significant advancements have been made in the definition of innovative “minimal-damage structures,” chasing the need for more resilient societies against extreme seismic events. In this context, moment resisting frames (MRFs) equipped with self-centering damage-free (SCDF) devices in column bases and beam-to-column joints represent a viable solution to improve structural resilience and damage reduction. However, the extensive use of these devices significantly increases complexity and costs compared to conventional structures, thus limiting their practical application. To overcome this drawback, current research works are focusing on the definition of effective placement for SCDF devices, maximizing their beneficial effect on the seismic response and controlling their impact on the overall structural complexity. Within this context, the present study investigates the influence of the placement of SCDF devices in a steel MRF. An eight-story MRF is designed, and 50 configurations with different locations of SCDF joints are considered. Numerical models are developed in OpenSees, and non-linear static push-pull and incremental dynamic analyses (IDAs) are carried out. The influence of the placement of SCDF devices is assessed by considering residual and peak interstory drifts, residual top story drifts, peak story accelerations, and the total dissipated energy as performance parameters. The results of IDAs for a seismic intensity corresponding to the ultimate limit state (ULS) are analyzed and compared, and fragility curves are successively derived for some relevant configurations. The paper provides insights and observations to understand how including a different number of SCDF BCJs at different stories affects the seismic response.

## KEYWORDS

residual drifts, seismic performance, self-centering damage-free connections, steel moment resisting frames, structural resilience

This is an open access article under the terms of the [Creative Commons Attribution-NonCommercial-NoDerivs](https://creativecommons.org/licenses/by-nc-nd/4.0/) License, which permits use and distribution in any medium, provided the original work is properly cited, the use is non-commercial and no modifications or adaptations are made.

© 2022 The Authors. *Earthquake Engineering & Structural Dynamics* published by John Wiley & Sons Ltd.

## 1 | INTRODUCTION

Traditional seismic design methods suggested by current codes<sup>1–3</sup> are based on energy dissipation related to construction damage following the “capacity design” philosophy. This implies large direct (e.g., casualties, repair cost) and indirect (e.g., downtime) losses<sup>4</sup> as a consequence of “rare” (i.e., high intensity) seismic events, and can lead to large residual deformations, thus impairing buildings’ repairability<sup>5</sup>. This situation strongly affects the overall resilience of communities subjected to extreme seismic events, especially when the damaged structures include strategic facilities such as hospitals and fire stations that must remain operational in the aftermath of a damaging earthquake. In this direction, nowadays earthquake engineering is facing an extraordinarily challenging era coping with the task of providing low-cost, thus more widely affordable, high-seismic-performance structures capable of sustaining the design earthquake intensity with limited socio-economical losses<sup>6</sup>. Within this context, many recent research studies focused on the development of innovative seismic-resilient structures chasing the objectives of minimizing both seismic damage and repair time, hence allowing the definition of structures able to return to the undamaged, fully functional condition in a short time<sup>7,8</sup>. For this purposes, innovative technologies based on supplemental damping devices<sup>9–12</sup> and base isolation systems<sup>13,14</sup> have been widely investigated in the last few decades, and the application of some of these technologies is nowadays mature and becoming popular in many earthquake-prone regions.

Among others, for steel moment resisting frames (MRFs), one viable solution is represented by the use of damage-free joints based on friction devices (FDs). Grigorian et al.<sup>15</sup> pioneered the first FD to be included in beam-to-column joints (BCJs) consisting of slotted bolted connections, which dissipate the seismic input energy through friction during cyclic loads. Successively, the application of FDs in BCJs has been widely studied by several authors. Latour et al.<sup>16</sup> experimentally and numerically investigated two configurations of symmetric removable FDs for low-damage BCJs, observing a satisfactory overall performance with a stable and predictable hysteretic response and no yielding of the structural members. Khoo et al.<sup>17</sup> and Borzouie et al.<sup>18</sup> proposed and experimentally tested asymmetric friction connections showing their cyclic behavior, providing design recommendations, and highlighting the limitations for their implementation. The development of several systems for BCJs with FDs also led to tailored design methods for this type of structure. Nastri et al.<sup>19</sup> examined three design criteria based on non-linear static and dynamic analyses. The results highlighted the benefits deriving by the use of FDs in BCJs, the effectiveness of the proposed design strategies, and the possibility of decoupling the overall strength and stiffness of the structure. Additional studies focused on the friction properties of innovative materials to be used within FDs. Among others, Latour et al.<sup>20</sup> carried out an experimental campaign on FDs considering steel plates coated by thermally sprayed aluminum as friction interface. The results showed that this material is characterized by a large and stable kinematic friction coefficient, hence allowing better performances compared to other previously tested metallic or rubber materials<sup>21</sup>. Although it has been demonstrated that the use of BCJs equipped with FDs can effectively protect the frame components from local damage, global damage can still be observed in the form of large residual deformations, hence jeopardizing both the operativity and repairability of such structures. McCormick et al.<sup>5</sup> suggested a threshold of 0.5% as a permissible residual drift to ensure the building’s repairability. Conversely, the FEMA P58-1<sup>22</sup> recommends a limit value of 0.2% to ensure that no structural realignment is necessary. However, independently of the threshold value imposed, it has been highlighted on several occasions that there is a significant need for structural systems able to limit residual deformations. This issue has been tackled by several research studies introducing elastic restoring forces able to regulate the self-centering capability of the structure, and one possible solution for framed structures is the inclusion of self-centering damage-free (SCDF) devices at BCJs. For example, Ricles et al.<sup>23</sup> proposed and numerically investigated a type of self-centering MRF equipped with post-tensioned (PT) connections obtained by post-tensioning beams to columns through high strength strands. Kim and Christopoulos<sup>24</sup> proposed and numerically tested a design procedure for such structures, demonstrating their superior seismic performance. Additional studies<sup>25,26</sup> have also focused on the use of alternative dissipative and easy-to-replace devices within self-centering steel PT connections. Furthermore, it has been shown that protecting column bases (CBs) from damage is an essential requirement for seismic-resilient structures. To this scope, several research studies proposed and investigated the use of SCDF connections in CBs<sup>27–30</sup>. Freddi et al.<sup>27,28</sup> presented and experimentally investigated a rocking damage-free steel CB, which uses PT high-strength steel bars to control the rocking behavior, FDs to dissipate the seismic energy, and a circular steel plate with rounded edges as a rocking base. A similar configuration was proposed by Kamperidis et al.<sup>29</sup> while using a square rocking base and hourglass shape steel yielding devices. Lately, Latour et al.<sup>30</sup> investigated and experimentally tested a sliding hinge joint used for CBs and equipped with PT threaded bars and disk springs to introduce joint restoring forces. It is noteworthy that most of the past studies<sup>23,24,27</sup> have focused on the use of SCDF devices in all BCJs demonstrating the

advantages in terms of self-centering capabilities and damage-free behavior. Nevertheless, a drawback of these solutions is the complexity of the structural details. If, on the one hand, the use of SCDF devices in all the joints is expected to produce a fully damage-free and self-centering response, on the other hand, it may represent a limit to the practical application due to the increase of structural complexity. In this regard, two fundamental aspects need to be further investigated to promote the use in practice of such systems: (1) the definition of SCDF connections that can be easily fabricated and installed; (2) the effects of the design and placement of SCDF connections within the structure.

Current research studies are investigating the influence of the placement of SCDF devices within steel MRFs. Elettore et al.<sup>31,32</sup> demonstrated that the use of SCDF devices applied only at CBs effectively reduces the residual story drifts and protects the first-story columns from damage. However, the results suggested that this solution is effective for low-rise steel MRFs (i.e., four stories) while its effectiveness is reduced increasing the number of stories (i.e., eight stories)<sup>32</sup>. In this context, the present work investigates the effective placement of a limited number of SCDF devices applied in both CBs and BCJs, such that their contribution to improving the seismic performance of the structure is maximized.

An eight-story three-bays MRF is selected as a case-study structure, and 50 different configurations with different locations of SCDF devices are considered. The SCDF CB and BCJ connections considered in this study are based on the one proposed and experimentally investigated by Latour et al.<sup>30</sup>. The reference MRF is designed according to Eurocode 8<sup>1</sup> requirements, while SCDF CBs and BCJs are designed by following a tailored design procedure. The flooring system of the conventional MRF is based on a disconnected steel-concrete slab in order to avoid the composite actions<sup>1</sup> with the beams. The slab is disconnected from the BCJs by the presence of gaps between the slab and the columns at the beam-to-column connections. This strategy is suggested and compliant with the Eurocode 8<sup>1</sup> provisions. Conversely, the flooring system of the self-centering MRFs is based on a disconnected and discontinuous steel-concrete slab in order to avoid damage due to the gap opening and closing mechanisms as done in previous studies<sup>33–35</sup>. The slab discontinuity is achieved by using two angle sections sliding on the beam framing perpendicularly to the columns and the slab reinforcing mesh is discontinued at the level of the angles. The slab diaphragm eliminates beam shortening, and so, the internal axial forces in the beams are not affected by the interaction with the slab<sup>35</sup>. Finite element (FE) models are developed in OpenSees<sup>36</sup> for all case-study configurations. Non-linear static push-pull (i.e., cyclic) analyses are performed by applying a lateral force distribution based on the first mode of vibration to monitor the local behavior of the structure (e.g., the formation of plastic hinges; the behavior of SCDF joints; and the elastic behavior of the panel zones)<sup>37</sup>. Additionally, non-linear dynamic analyses are performed in an incremental dynamic analysis (IDA)<sup>38</sup> fashion to evaluate the seismic response of each configuration. IDAs are carried out on a set of 30 ground motion records selected using REXEL<sup>39</sup> and accounting for the influence of the uncertainty related to the earthquake input (i.e., the record-to-record variability). Average spectral acceleration ( $avgSa$ ) in the range of periods of the stiffest and more flexible structure is assumed as intensity measure (IM). The seismic response of the different configurations is compared and analyzed by considering several engineering demand parameters (EDPs), such as residual and peak interstory drifts, residual top story drifts, and peak story accelerations. The results of IDAs for a seismic intensity corresponding to the ultimate limit state (ULS) are presented and compared for all the configurations. Fragility curves are successively derived for some of the most effective configurations providing the probability of exceeding a specified failure condition given the seismic intensity<sup>40</sup>. The results of the study provide useful insights and recommendations on the effective placement of SCDF BCJs and on their effect on the main global EDPs conventionally used to represent the seismic performance of building structures.

The paper is organized as follows: Section 2 describes the SCDF joint considered, its behavior, and the tailored design procedure developed; Section 3 describes the design of the case-study structure and the 50 additional configurations equipped with SCDF CBs and BCJs; Section 4 describes the numerical modeling strategy while Section 5 describes, analyzes, and critically compares the results obtained from the non-linear static push-pull analyses and the IDAs.

## 2 | SELF-CENTRING DAMAGE-FREE JOINT

The SCDF connection proposed and experimentally tested by Latour et al.<sup>30</sup> is considered for the design and analysis of a case-study structure; however, the obtained results can be extended and generalized to any other technology showing a similar flag-shape moment-rotation behavior. Figure 1 shows two schematic representations of the SCDF CB and BCJ considered in this work. The structural elements, i.e., upper and lower part of the first story columns for CBs, and beams and columns for BCJs, are connected by a combination of FDs, which dissipate the seismic input energy through the alternate slippage of the surfaces in contact, and a self-centering system, which, together with the gap opening mechanism, controls the self-centering behavior of the connection.

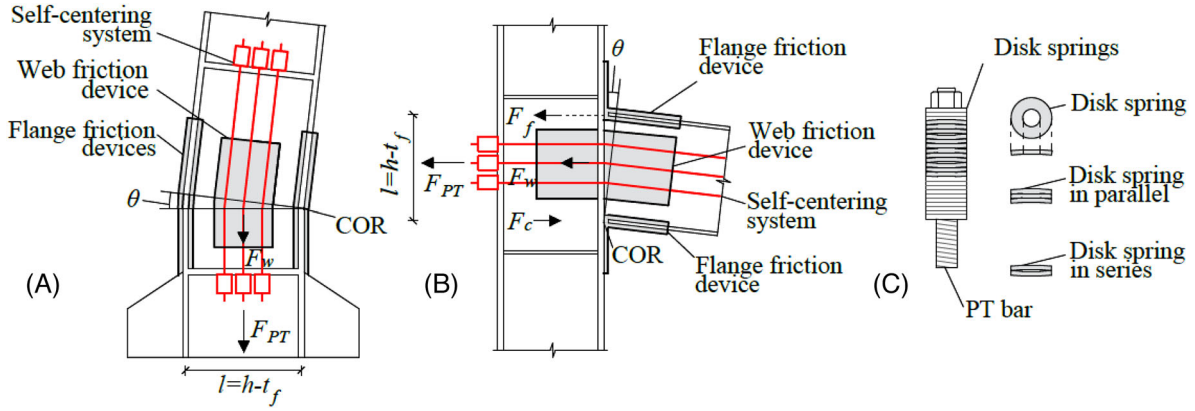


FIGURE 1 Self-centering damage-free (SCDF) connection for: (A) column bases (CBs), (B) beam-to-column joints (BCJs). (C) Details of the self-centering system (i.e., post-tensioned bars and disk springs)

Figure 1A and B show the SCDF connections, including the FDs in both web and flanges, the self-centering system, the center of rotation (COR), the forces developed during the rocking behavior, and the lever arms of the forces with respect to the COR. FDs consist of steel plates with oversized and slotted holes, equipped with friction pads and clamped together with pre-loaded bolts. The self-centering system is composed of PT bars arranged in series with disk springs allowing the definition of an ideal stiffness–resistance combination. Disk springs are assembled into two different configurations with different functions within the self-centering system (Figure 1C). The disk springs in parallel control the yielding resistance of the self-centering system while the disk springs in series control its stiffness. Additionally, it is worth mentioning that the structural configuration of the SCDF devices applied to the external and internal BCJs (i.e., with respectively one and two convergent beams) is slightly different. While a representation of the external SCDF BCJs is shown in Figure 1B, in the internal SCDF BCJs, the PT bars cross the joint uninterruptedly from one side to the other. Further details on the structural configuration of the SCDF connection can be found in Latour et al.<sup>30</sup> and Elettore et al.<sup>31</sup>.

## 2.1 | Forces in the components

The design of SCDF joints is based on the knowledge of the design forces developed in the connection during the gap-opening phase (Figure 1A and B). The forces in the FDs in the web ( $F_w$ ) and flanges ( $F_f$ ) are defined as follow:

$$F_w = \mu \cdot n_s \cdot n_{bw} \cdot F_{p,w} \quad ; \quad F_f = \mu \cdot n_s \cdot n_{bf} \cdot F_{p,f} \quad (1)$$

where  $\mu$  is the design value of the friction coefficient;  $n_s$  the number of friction surfaces (i.e., two in the considered configuration);  $n_{bw}$  and  $n_{bf}$  are the numbers of bolts respectively in the web and the flanges; and  $F_{p,w}$  and  $F_{p,f}$  are the post-tensioning forces on each bolt respectively in the web and the flanges.

The force in the PT bars ( $F_{PT}$ ) is defined as follow:

$$F_{PT} = F_{PT,0} + \Delta F_{PT} \quad ; \quad F_{PT,0} = n_{PT} \cdot F_{p,PT} \quad ; \quad \Delta F_{PT} = K_{eq} \cdot \Delta l_{avg,PT} \quad (2)$$

where  $F_{PT,0}$  is the initial post-tensioning force in the PT bars;  $\Delta F_{PT}$  the extra force occurring in the PT bars during the gap opening phase;  $n_{PT}$  the total number of PT bars;  $F_{p,PT}$  the post-tensioning force on each PT bar;  $K_{eq}$  the equivalent stiffness of the whole system composed by PT bars and disk springs; and  $\Delta l_{avg,PT}$  is the average elongation of the PT bars, corresponding to the maximum target rotation ( $\theta_t$ ) and considering that they are symmetrically placed with respect to the center of the section.  $K_{eq}$  can be calculated as follow:

$$K_{eq} = n_{PT} \cdot \frac{K_{PT} \cdot K_{DS}}{K_{PT} + K_{DS}} \quad ; \quad K_{PT} = \frac{E_{PT} \cdot A_{s,res,PT}}{L_{PT}} \quad ; \quad K_{DS} = \frac{n_{par}}{n_{ser}} \cdot K_{DS1} \quad (3)$$

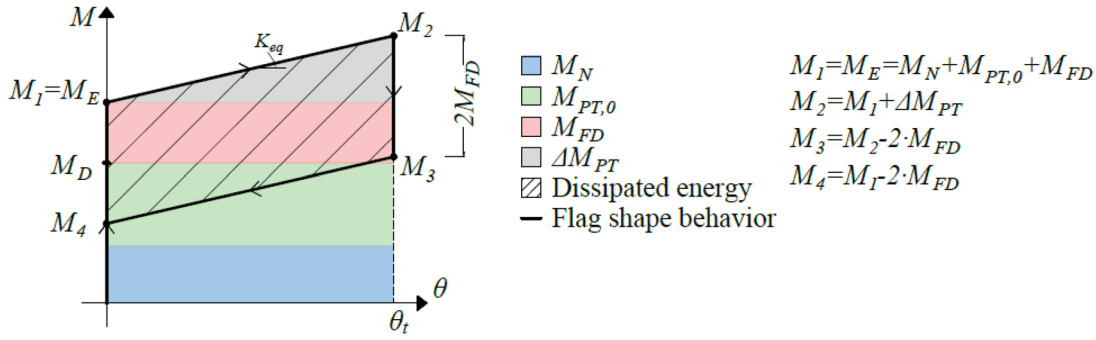


FIGURE 2 Moment–rotation behavior of the self-centering damage-free (SCDF) joint; moment contributions; flag-shape hysteretic behavior

where  $K_{PT}$  is the stiffness of a single PT bar;  $K_{DS}$  the stiffness of the set of disk springs;  $E_{PT}$  the elastic modulus of the PT bars;  $A_{s,res,PT}$  the resistance area of a PT bar;  $L_{PT}$  the length of the PT bars;  $n_{par}$  and  $n_{ser}$  are respectively the numbers of disk springs arranged in parallel and in series; and  $K_{DSI}$  is the stiffness of the single disk spring.  $\Delta l_{avg,PT}$  is evaluated considering  $\theta_t$  equal to 40 mrad, which is the benchmark rotation established by AISC 341-16<sup>2</sup> for BCJs in Special MRFs and can be calculated as

$$\Delta l_{avg,PT} = \theta_t \cdot (l/2) \quad (4)$$

where  $l = h - t_f$  with  $h$  and  $t_f$  being respectively the height and flange's thickness of the cross-section of the structural element.

## 2.2 | Moment–rotation relationship

Two phases characterize the behavior of the connection: (1) the closed phase; and (2) the gap-opening phase. The following assumptions are made for the definition of the moment–rotation relationship: (1) the axial force in the connection due to external forces is constant and equal to  $N_{Ed}$ , for example, the gravity force in the columns; (2) the forces in the FDs for web ( $F_w$ ) and flanges ( $F_f$ ) are entirely developed in the closed phase, and their contribution remains constant during the gap opening phase (i.e., rigid-plastic behavior); and (3) in the PT bars the initial post-tensioning force ( $F_{PT,0}$ ) is constant, while the additional force ( $\Delta F_{PT}$ ) occurs due to the gap opening and linearly varies with the joint's rotation.

The moments' contributions for the definition of the moment–rotation behavior of the connection are shown in Figure 2 and can be calculated, with respect to the COR, as follow:

$$M_N = N_{Ed} \cdot (l/2) \quad ; \quad M_{PT,0} = F_{PT,0} \cdot (l/2) \quad ; \quad M_{FD} = M_{FD,w} + M_{FD,f} = F_w \cdot (l/2) + F_f l \quad (5a)$$

$$\Delta M_{PT} = \Delta F_{PT} \cdot (l/2) = K_{eq} \cdot \theta_t \cdot (l/2)^2 \quad (5b)$$

where  $M_N$  is the moment developed by the external axial force;  $M_{PT,0}$  the moment developed by the initial post-tensioning force;  $M_{FD}$  the total moment developed by the FDs in the web ( $M_{FD,w}$ ) and the flanges ( $M_{FD,f}$ ); and  $\Delta M_{PT}$  is the moment developed by the additional force as a consequence of the gap opening. Therefore, the decompression moment ( $M_D$ ) and the elastic resisting moment ( $M_E$ ) can be calculated as follow:

$$M_D = M_N + M_{PT,0} \quad ; \quad M_E = M_N + M_{PT,0} + M_{FD} \quad (6)$$

Figure 2 shows the flag-shape moment–rotation behavior of the SCDF joints with the four fundamental values of the moment, namely, the max and min moment at zero ( $M_1, M_4$ ) and target rotation  $\theta_t$  ( $M_2, M_3$ ). Further details on the validation of the moment–rotation relationship of the SCDF connection can be found in Elettore et al.<sup>31</sup>

### 2.3 | Design procedure

The design procedure of the SCDF connection requires as input parameters: (1) the cross-section properties of the structural element; (2) the design forces, i.e., max and min axial force ( $N_{Ed,min}$ ,  $N_{Ed,max}$ ) and bending moment ( $M_{Ed}$ ) in the structural element due to the seismic combination for the ULS; and (3) the yielding moment of the structural element ( $M_y$ ). The objective of the design procedure is to satisfy at the same time three main conditions: (1) no yielding of the structural element; (2) self-centering behavior of the structure; and (3) bending moment corresponding to the gap opening higher than the one defined by Eurocode 8<sup>1</sup> for resistance checks. The aforementioned conditions can be summarized in the following system of inequalities:

$$\begin{cases} M_2 < M_y \\ M_A > 0 \rightarrow M_D > M_{FD} \\ M_1 > M_{Ed} \end{cases} \quad (7)$$

Partial safety factors are introduced to account for the random variability of the friction coefficient ( $\gamma_\mu$ ) and the post-tensioning forces ( $\gamma_{PT}$ ). Based on previous tests on friction materials<sup>41</sup>,  $\gamma_\mu$  is assumed equal to 1.39 while  $\gamma_{PT}$  is assumed equal to 1.2 according to EN 1090-2<sup>42</sup>. It is worth mentioning that the safety factor used for FDs accounts for both uncertainties (i.e.,  $\alpha_{FD} = \gamma_\mu \times \gamma_{PT} = 1.67$ ).

The three conditions in Equation (7) must consider the unfavorable combination of axial load ( $N_{Ed,max}$  or  $N_{Ed,min}$ ) and safety factors ( $\alpha_{FD}$ ,  $\gamma_{PT}$ ) as follows: (1) for the no yielding condition –  $N_{Ed,max}$ ,  $\alpha_{FD}$ , and  $\gamma_{PT}$ ; (2) for the self-centering condition –  $N_{Ed,min}$ , and  $\alpha_{FD}$ ; and (3) for the gap opening condition –  $N_{Ed,min}$ . A simple rearrangement of Equation (7) leads to:

$$\begin{cases} \gamma_{PT} \cdot M_{PT,0} + \alpha_{FD} \cdot M_{FD} + \Delta M_{PT} < M_y - M_{N_{Ed,max}} \\ M_{PT,0} - \alpha_{FD} \cdot M_{FD} > -M_{N_{Ed,min}} \\ M_{PT,0} + M_{FD} > M_{Ed} - M_{N_{Ed,min}} \end{cases} \quad (8)$$

Therefore, the design procedure consists of solving the system of three inequalities with three unknown variables (i.e.,  $M_{PT,0}$ ,  $M_{FD}$ ,  $\Delta M_{PT}$ ). Deriving  $M_{PT,0}$ ,  $M_{FD}$ , and  $\Delta M_{PT}$  from Equation (8), and imposing that the moment due to the FDs ( $M_{FD}$ ) is equally distributed among the FDs of web and flanges (i.e.,  $M_{FD,w} = M_{FD,f} = M_{FD}/2$ ) is possible to derive the properties of each component of the device, i.e.,  $F_{PT,0}$ ,  $F_w$ ,  $F_f$ , and  $K_{eq}$  by Equations (5). Successively, the number of bolts of the FDs for web and the flanges ( $n_{bw}$ ,  $n_{bf}$ ) and the number of PT bars ( $n_{PT}$ ) can be designed by choosing the diameter and the class of bolts and PT bars, inverting Equations (1) and (2) and ensuring that the post-tensioning force in each bolt ( $F_{p,w}$ ,  $F_{p,f}$ ) and PT bar ( $F_{p,PT}$ ) is smaller than the maximum post-tensioning force ( $F_{p,max}$ ) defined in Eurocode 3-Part 8<sup>43</sup>.

The number of disk springs in parallel ( $n_{par}$ ) is calibrated based on the yielding force of the PT bars as follow:

$$F_{y,DS} \geq F_{y,PT} \rightarrow n_{par} = \frac{F_{y,PT}}{F_{y,DS1}} = \frac{A_{s,res,PT} \cdot f_y}{F_{y,DS1}} \quad (9)$$

where  $A_{s,res,PT}$  is the resisting area of a PT bar;  $f_y$  the yielding stress of the steel used for the PT bars; and  $F_{y,DS1}$  is the yielding strength of a single disk spring. The number of disk springs in series ( $n_{ser}$ ) is calculated based on Equation (3).

The no yielding of the PT bars and disks springs in parallel needs to be verified. A tensile resistance check is carried out considering the individual elongation of the PT bars to verify that the total axial force in the PT bars and in the disk springs in parallel (i.e.,  $F_{PT}$  from Equation 2) does not exceed their yielding capacity (i.e.,  $F_{y,PT}$  and  $F_{y,DS}$ ).

In conclusion, to ensure the capacity design of the SCDF connection against the shear mechanism, a shear resistance check is carried out verifying that the forces in the FDs in the web and flanges ( $F_w$ ,  $F_f$ ) do not exceed the shear force associated with the yielding moment of the structural element ( $V_{Ed} = M_y/L_0$  where  $L_0$  is the shear length).

## 3 | CASE-STUDY STRUCTURES

Figure 3 shows the eight-story steel building selected as case-study. It has interstory heights of 3.50 m for the first level and 3.20 m for the others. The plan layout consists of five and three bays respectively in  $x$ - and  $y$ -direction with a constant span

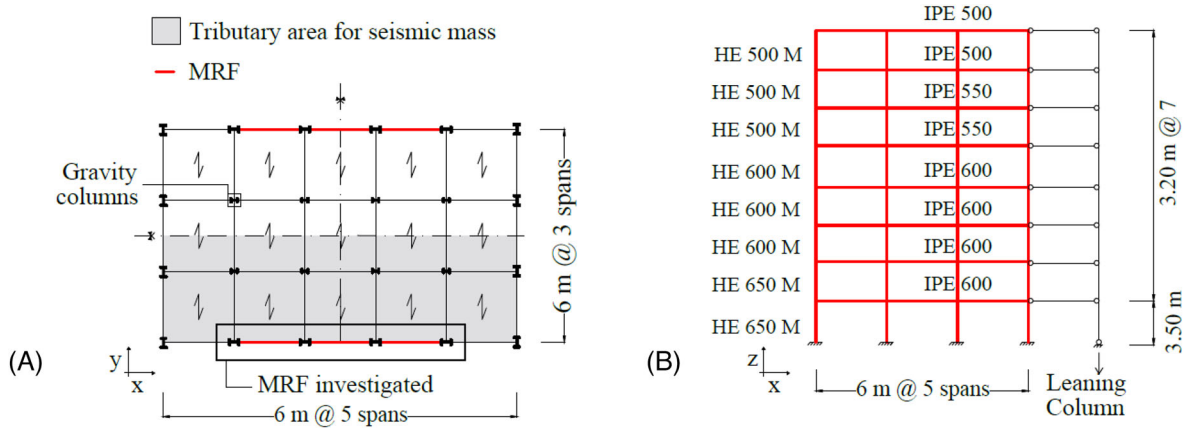


FIGURE 3 (A) Plan view, and (B) elevation view of the case-study frame

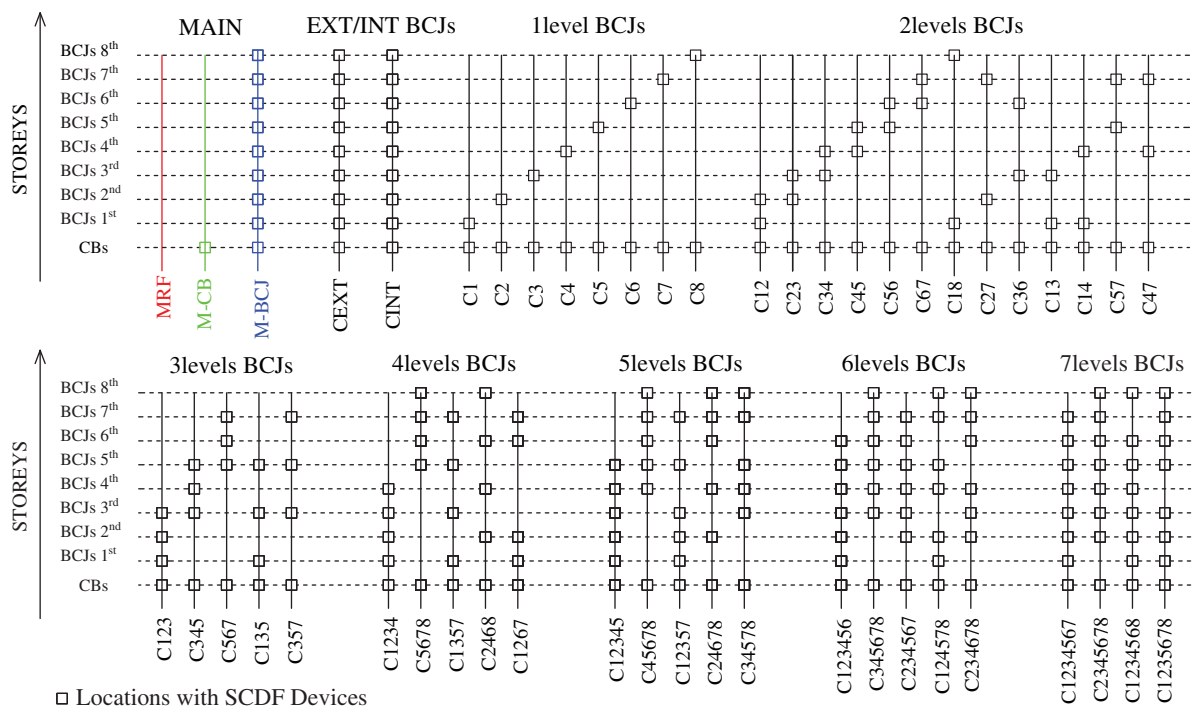


FIGURE 4 Investigated configurations

of 6.0 m. The seismic resisting system consists of perimeter MRFs, while the interior part is composed of gravity frames with “pinned” connections. The present study focuses on the assessment of one of the perimeter MRFs in the  $x$ -direction.

To investigate the influence of SCDF joints' location on the seismic performance of the MRF, 50 structural configurations are considered, as illustrated in Figure 4. Each configuration is exemplified by a vertical line (i.e., 50 total vertical lines) with nine levels along the height which respectively represent the ground floor and the eight stories. A gray square is placed in those levels where all the joints (i.e., internal and external) are equipped with SCDF devices. The three reference configurations consist of: (1) the MRF with conventional CBs and full-strength BCJs (indicated as MRF); (2) the equivalent MRF equipped with the SCDF CBs (indicated as M-CB); and (3) the equivalent MRF equipped with SCDF connections in both CBs and all BCJs (indicated as M-BCJ). Furthermore, 45 additional configurations (indicated as C) are defined considering SCDF CBs and different layouts of SCDF BCJs. For example, C345 indicates the configuration with SCDF CBs and three levels of SCDF BCJs applied respectively in all internal and external joints belonging to stories three, four, and five. Additionally, the equivalent MRF equipped with SCDF connections in CBs and only external BCJs or internal BCJs are considered (indicated respectively as CEXT and CINT).

**TABLE 1** Design input for the self-centering damage-free column bases (CBs)

	Section profile	$N_{Ed,min}$ (kN)	$N_{Ed,max}$ (kN)	$M_{Ed}$ (kNm)	$M_y$ (kNm)
CB-EXT	HE 650 M	-1556	+2749	2025	4872
CB-INT	HE 650 M	+855	+863	2138	4872

CB-EXT, column base external; CB-INT, column base internal.

### 3.1 | Design of the conventional moment resisting frame

The conventional MRF (i.e., MRF) is designed according to Eurocode 8<sup>1</sup>. Steel grades S275 and S355 are used respectively for beams and columns. A disconnected steel-concrete slab, compliant with the Eurocode 8<sup>1</sup> provisions, is considered, as previously discussed. The considered permanent and live gravity loads are  $G_{k,floor} = 4.5$  kN/m<sup>2</sup>,  $G_{k,cladding} = 2$  kN/m, and  $Q_k = 2$  kN/m<sup>2</sup>. The design earthquake at the ULS (probability of exceedance of 10% in 50 years) is defined considering the type 1 elastic response spectrum with a peak ground acceleration of 0.35 g, soil type C, and a building's importance factor equal to 1. The building is characterized by plan and elevation regularity. The behavior factor ( $q$ ) is evaluated according to the provisions of the Eurocode 8<sup>1</sup> for MRFs in DCH, hence assumed equal to 6.5. The structure has non-structural elements fixed in a way so as not to interfere with structural deformations. Therefore, the interstory drift limit for the damage limit state (DLS; probability of exceedance of 10% in 10 years) is assumed as 1%, accordingly with the Eurocode 8<sup>1</sup>. Beams' and columns' sections are reported in Figure 3B, and panel zones are stiffened with doubler plates with a thickness equivalent to the column's web to ensure the formation of plastic hinges at beams' ends only. The mass of each story is evaluated based on the seismic combination of the Eurocode 8<sup>1</sup> considering the tributary area of the investigated MRF, as shown in Figure 3A.

### 3.2 | Design of the self-centering moment resisting frames

The self-centering MRFs (i.e., M-CB, M-BCJ, C-) are obtained, including properly designed SCDF connections at specific locations of the conventional MRF. For these frames, a disconnected and discontinuous steel-concrete slab<sup>33–35</sup> is considered, as previously discussed. This solution allows avoiding damage to the slab due to the gap opening and closing mechanisms in the SCDF BCJs. Moreover, it ensures that the internal axial forces in the SCDF BCJs are controlled only by the PT force variation related to the rocking behavior.

#### 3.2.1 | Design of the self-centering damage-free column bases (CBs)

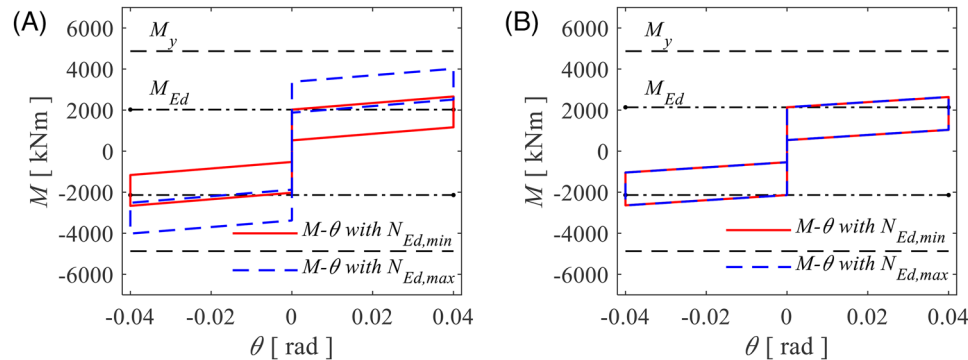
The SCDF CBs are designed following the procedure described in Subsection 2.3. It is worth reminding that the cross-section profile of columns is HE 650 M for story 1. Two different configurations of the CBs are defined: (1) for the external columns (CB-EXT), which are subjected to the high variability of the axial force during the seismic event; and (2) for the internal columns (CB-INT). The design actions are derived based on a linear static analysis with loads defined according to the lateral force method of the equivalent frame with full-strength connections (i.e., the MRF). The max and min axial force ( $N_{Ed,min}$ ,  $N_{Ed,max}$ ) and the bending moment ( $M_{Ed}$ ) of the external and internal columns are taken from the seismic combination of the Eurocode 8<sup>1</sup> for the ULS. In order to avoid the yielding of the first story columns, their lower part is reinforced through 30 mm thick steel plates welded to the flanges. Therefore, the yielding moment of the column ( $M_y$ ) to be considered in the design procedure takes into account the strengthening provided by cover plates in the spliced region. The design input information for external and internal columns is reported in Table 1, where “-” stands for tension and “+” for compression. The friction coefficient ( $\mu$ ) is assumed equal to 0.53, which is the recommended dynamic friction coefficient value for material M4<sup>13</sup>. The following properties are chosen for the components of the SCDF CBs: HV M30 10.9 class bolts for web and flanges FDs, HV M39 10.9 class PT bars with a length of 1.7 m, disk springs with a yielding strength ( $F_{y,DSI}$ ) equal to 250 kN, and a stiffness ( $K_{DSI}$ ) of 96 kN/mm. The results of the design procedure obtained for external and internal columns are reported in Table 2.

Figure 5 shows the flag-shape behavior for CB-EXT and CB-INT. The dashed and dot-dashed black lines represent respectively the yielding moment of the structural element ( $M_y$ ) and the bending moment ( $M_{Ed}$ ) in the columns due



**TABLE 2** Design results for the external (EXT) and internal (INT) self-centering damage-free column bases (CBs)

	$n_{bw}$ (-)	$F_{p,w}$ [kN]	$n_{bf}$ (-)	$F_{p,f}$ [kN]	$n_{PT}$ (-)	$F_{p,PT}$ [kN]	$n_{par}$ (-)	$n_{ser}$ (-)	$K_{eq}$ (kN/mm)
CB-EXT	4	282	2	282	10	562	4	20	161.6
CB-INT	4	300	2	300	6	568	4	15	126.8

**FIGURE 5** Moment-rotation behavior considering  $N_{Ed,min}$  and  $N_{Ed,max}$  for: (A) column base external (CB-EXT), (B) column base internal (CB-INT)**TABLE 3** Design input for the self-centering damage-free beam-to-column joints (BCJs)

	Section profile	$N_{Ed}$ (kN)	$M_{Ed}$ (kNm)	$M_y$ (kNm)
BCJs 1–4	IPE 600	0	455	810
BCJs 5–6	IPE 550	0	331	640
BCJs 7–8	IPE 500	0	188	508

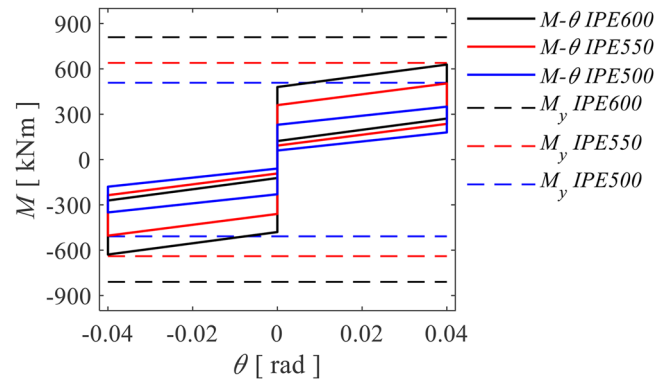
to the seismic combination at the ULS. The red and blue lines represent the characteristic flag-shape behavior calculated respectively with the max ( $N_{Ed,min}$ ) and min ( $N_{Ed,max}$ ) axial forces. Figure 5A refers to the external columns, which, being subjected to the high variability of axial force during the seismic event, show two significantly different flag-shape curves. Conversely, Figure 5B refers to internal columns, where, being the compression for both  $N_{Ed,min}$  and  $N_{Ed,max}$  almost identical, show coincident flag-shape curves. For both cases, the following considerations can be made: (1)  $M_1$  is larger than  $M_{Ed}$ ; (2)  $M_2$  is always smaller than  $M_y$ , hence avoiding yielding of the column; and (3)  $M_4$  is larger than zero hence ensuring the self-centering capability of the connection. Therefore, it is shown how the design procedure allows satisfying the aforementioned conditions with a safety margin due to the adoption of two safety factors  $\alpha_{FD}$  and  $\gamma_{PT}$ .

### 3.2.2 | Design of the self-centering damage-free beam-to-column joints (BCJs)

The SCDF BCJs are designed following the procedure described in Subsection 2.3. It is worth reminding that the cross-section profiles of the beams are: IPE 600 for stories one to four, IPE 550 for stories five and six, and IPE 500 for stories seven and eight. In this case, six different configurations of SCDF joints are defined: one for the internal BCJs (BCJ-INT) and one for the external BCJs (BCJ-EXT) for each selected cross-section. The design procedure is the same followed for CBs with two main differences: (1) beams are not subject to externally imposed axial forces (i.e.,  $N_{Ed,min} = N_{Ed,max} = 0$ ); (2) the yielding moment of the beam ( $M_y$ ) to be considered in the design procedure is the nominal one since beams are not reinforced. The design input information for the three cross-sections is reported in Table 3.  $K_{eq}$  is calculated differently for the internal and external BCJs, due to their different structural configuration. In fact, while for BCJ-EXT  $K_{eq}$  can be simply obtained by inverting Equation (5b) as for CBs, for BCJ-INT the PT bars are uninterrupted within the joint, hence the average elongation of the PT bars ( $\Delta l_{av,PT}$ ) in Equation (5b) must be considered proportional to two times the target rotation ( $2 \cdot \theta_t$ ). The friction coefficient ( $\mu$ ) and the properties chosen for the components of the BCJ are the same as the

**TABLE 4** Design results for the external (EXT) and internal (INT) self-centering damage-free beam-to-column joints (BCJs)

	$n_{bw}$ (-)	$F_{p,w}$ (kN)	$n_{bf}$ (-)	$F_{p,f}$ [kN]	$n_{PT}$ (-)	$F_{p,PT}$ (kN)	$n_{par}$ (-)	$n_{ser}$ (-)	$K_{eq}$ (kN/mm)
BCJs 1–4 (EXT)	4	73	2	73	4	259	3	23	440.3
BCJs 1–4 (INT)	4	73	2	73	4	259	3	49	220.2
BCJs 5–6 (EXT)	4	59	2	59	4	212	3	20	506.4
BCJs 5–6 (INT)	4	59	2	59	4	259	3	43	253.2
BCJs 7–8 (EXT)	4	42	2	42	4	150	3	20	512.3
BCJs 7–8 (INT)	4	42	2	42	4	259	3	42	256.1

**FIGURE 6** Moment–rotation behavior for beam-to-column joints (BCJs) at: stories one to four (black line), stories five and six (red line), stories seven and eight (blue line)

CBs except for PT bars which are HV M36 10.9. The results of the design procedure obtained for the external and internal SCDF BCJs considering the three cross-sections are reported in Table 4.

Figure 6 shows the flag-shape behavior respectively for BCJ 1–4, BCJ 5–6, and BCJ 7–8. In this case, the relationship obtained for BCJ-EXT and BCJ-INT is the same. This is achieved by calibrating the number of PT bars and disk springs necessary to obtain the design value of  $K_{eq}$ . It is possible to see that the maximum moment of the flag-shape behavior is reduced while reducing the dimension of the beams' sections, thus with their yielding moment.

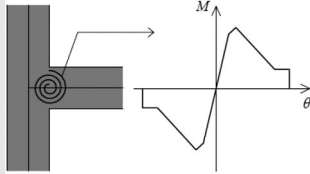
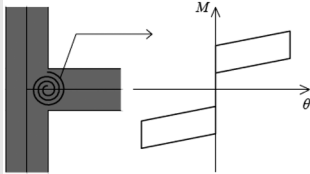
## 4 | FINITE ELEMENT MODELING

### 4.1 | Modeling of the conventional moment resisting frame

As only one of the perimeter MRFs in the  $x$ -direction is considered as a case-study structure, a two-dimensional non-linear FE model of the investigated MRF is developed in OpenSees<sup>36</sup>. The story masses are assigned considering the tributary area of the MRF (i.e., half of the total area as shown in Figure 3B). The FE model accounts for plastic hinges at beams' ends and considers conventional CBs connections. Table 5 summarizes the main characteristics of the conventional MRF model.

The “Steel01” material<sup>36</sup> with 275 and 355 MPa yield strength is used for beams and columns, respectively. A 0.2% post-yield stiffness ratio is used in both cases. Beams are modeled based on a lumped plasticity approach,<sup>44</sup> which, conversely to the distributed plasticity, has the advantage of indirectly accounting for local buckling. The internal part of the beams is modeled as an elastic element (“element elasticBeamColumn”<sup>36</sup>) while zero-length non-linear rotational springs (“element zeroLength”<sup>36</sup>) are placed at beams' ends to simulate the formation of plastic hinges. The rotational springs are defined with a bilinear hysteretic moment–rotation behavior (“uniaxialMaterial Bilinear”<sup>36</sup>) based on the modified Ibarra–Krawinkler deterioration model<sup>45</sup> implemented as suggested by Lignos and Krawinkler<sup>46</sup>. Columns are modeled as non-linear elements with distributed plasticity (“element nonlinearBeamColumn”<sup>36</sup>) computed in six integration points where fiber sections are defined to capture the interaction between the axial force and the bending moment. Each fiber section

**TABLE 5** Characteristics and differences between the conventional MRF and the self-centering MRF models

Model	Conventional MRF (i.e., MRF)	Self-centering MRFs (i.e., M-CB, M-BCJ, C-)
CBs	Fixed CBs (distributed plasticity for columns)	SCDF-CBs (advanced model for SCDF joints - Subsection 4.2)
Beams' ends	Plastic hinges (yielding/buckling) rotational springs with bilinear hysteretic moment-rotation behavior based on the modified Ibarra-Krawinkler deterioration model 	SCDF-BCJ (no yielding/no buckling) simplified model for SCDF joints ( Subsection 4.2): rotational springs with a flag-shape moment-rotation behavior obtained from the design procedure 
Slab	Disconnected steel-concrete slab	Disconnected and discontinuous steel-concrete slab
Damping	Advanced Rayleigh damping model based on the tangent stiffness	
Panel zones	Scissor model	

BCJ, beam-to-column joint; CB, column base; MRF, moment resisting frame; SCDF, self-centering damage-free.

is discretized into eight and four fibers, respectively, for web and flanges. The stiffness of the section is defined considering both the contributions of axial and shear stiffnesses through the “section aggregator”<sup>36</sup>. The panel zones are modeled based on the “Scissor” model<sup>47</sup>, according to which the behavior of the panel zone can be modeled as four rigid elements, two horizontal and two vertical, connected to a single hinge in the center. The central hinge is modeled with two zero-length rotational springs (“element zeroLength”<sup>36</sup>): one for the panel shear contribution and the other for the column flange bending contribution. The rigid slab behavior is modeled by imposing the same horizontal displacements between nodes belonging to the same story (“equalDOF”<sup>36</sup>). Geometric non-linearities are considered in the elements of the MRF (“geomTransf PDelta”<sup>36</sup>). Additionally, in order to consider the  $P-\Delta$  effects related to the gravity frame, a leaning column is included in the structural model<sup>48</sup>. It is representative of the gravity columns belonging to the half area of the building’s plan; therefore, its flexural stiffness and cross-area are defined as the sum of the flexural stiffness and cross-area of the gravity columns that replaces. The leaning column is modeled as pinned at the base and uninterrupted along the height, and it is connected to the MRF through rigid trusses. Distributed and concentrated loads are applied on beams and columns considering the seismic combination of Eurocode 8<sup>1</sup>, while the corresponding masses are concentrated at beam-column intersections. Damping sources other than the hysteretic energy dissipation are modeled through the advanced Rayleigh damping model based on the tangent stiffness<sup>49,50</sup>. A variant stiffness matrix is considered and updated at each time step of the analysis, avoiding spurious damping forces during regimes of inelastic responses. The values of the mass-related and stiffness-related Rayleigh damping coefficients are evaluated for a damping factor of 3% considering the first and the second vibration modes, which together cover modal participation mass ratios equal to 89.6%.

## 4.2 | Modeling of the self-centering moment resisting frame and joints

Before going into the details of the model, it is worth highlighting that according to the design procedure described in Section 2, the SCDF connections (both for BCJs and CBs) are designed including capacity design criteria that allow protecting the adjacent members from damage (i.e., no inelastic behavior of the beams and base connection of the first story columns). Therefore, at SCDF joints’ locations, modeling considerations about beams’ and columns’ inelastic deformations, local buckling, and post-buckling behavior are not required. According to this, beams and columns behave elastically at SCDF joints’ locations, and plastic hinges are not included in the model.

A two-dimensional non-linear FE model of the self-centering MRF is developed in OpenSees<sup>36</sup>. The model has the same characteristics as the conventional MRF but includes the implementation of SCDF BCJs at beams’ ends (instead of the plastic hinges) and SCDF CBs (instead of the fixed nodes). An advanced and a simplified modeling strategy are proposed and developed in OpenSees<sup>36</sup> for the SCDF joints. As described in the following sections, the former is used for SCDF CBs

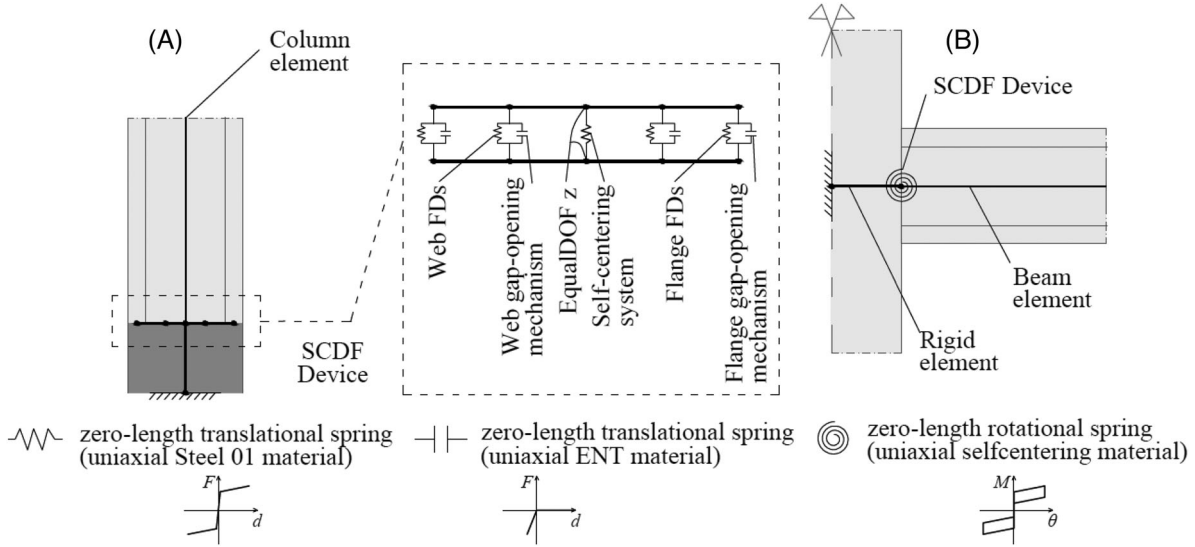


FIGURE 7 OpenSees models for external (EXT) beam-to-column joints (BCJs): (A) advanced; and (B) simplified modeling

while the latter is used for SCDF BCJs. Table 5 summarizes the main characteristics and differences between the model of the conventional MRF and the self-centering MRF.

The advanced modeling strategy is consistent with the work of Elettore et al.<sup>31,32</sup> on CBs in which a validation against experimental results was carried on, gaining confidence in the numerical results and the adopted numerical advanced modeling strategy. Figure 7A shows the advanced model for external SCDF BCJs. It consists of a sophisticated two-dimensional non-linear FE model where the rocking interface is modeled with eight rigid elements (“element elasticBeamColumn”<sup>36</sup>). The web and flanges FDs are modeled with four translational springs (“element zeroLength”<sup>36</sup>). They are defined by the “Steel01” material<sup>36</sup> considering a rigid initial behavior and a very low strain-hardening ratio to simulate the rigid plastic behavior, and a yield strength equal to the slippage forces in web and flanges FDs ( $F_w$  or  $F_f$ ) obtained from the design procedure. The rocking behavior is modeled with four translational springs (“element zeroLength”<sup>36</sup>). They are defined by the “Compression-no-tension (ENT)” material<sup>36</sup> and exhibit an elastic compression-no tension force-displacement behavior. The self-centering system composed of PT bars and disk springs is modeled by a single central translational spring (“element zeroLength”<sup>36</sup>). “Steel01” material<sup>36</sup> is adopted considering: (i) a stiffness equal to  $K_{eq}$ , (ii) a yielding force equal to the minimum between the yielding force of all PT bars and the yielding force of all disk springs in parallel, and (iii) an initial strain ( $s_{init}$ ) using the “Initial strain material”<sup>36</sup> in order to model the initial post-tensioning force ( $F_{PT,0}$ ). However, it is worth recalling that in the proposed configuration: PT bars are always subjected to tension forces and never to compression; and that, according to the design strategy described in Subsection 2.3 both the PT bars and the disk springs are not expected to yield under the earthquake intensities. The “EqualDOF” command is used to transfer the shear forces.

The simplified modeling strategy illustrated in Figure 7B consists of a non-linear rotational spring (“element zeroLength”<sup>36</sup>) allocated at beams’ ends and characterized by the flag-shape moment–rotation behavior (“uniaxialMaterial SelfCentering”<sup>36</sup>) of the SCDF connection. It is defined considering: (1) a rigid initial behavior; (2) the post-activation stiffness ( $K_2$ ); (3) the forward activation force ( $F_{act}$ ) corresponding to the moment at which the gap opening occurs, i.e.,  $M_1$ ; (4) the ratio of forward to reverse activation force ( $\beta$ ); and (5) no slippage and no bearing. The just mentioned parameters can be evaluated as follow:

$$K_2 = \frac{M_2 + M_1}{\theta_t} \quad ; \quad F_{act} = M_1 \quad ; \quad \beta = \frac{M_2 - M_3}{M_1} \quad (10)$$

where  $M_1$ ,  $M_2$ ,  $M_3$ , and  $\theta_t$  are the design parameters described in Subsection 2.2.

Figure 8 shows the moment–rotation behavior for BCJ-EXT at story one and BCJ-INT at story seven, including the comparison among the relationships obtained from the analytical and numerical models. The moment–rotation relationship obtained from the analytical model, described in Section 2, is reported with scatter points. The results of the numerical analyses performed on local models in OpenSees<sup>36</sup> are shown for the non-linear static and dynamic analyses, considering

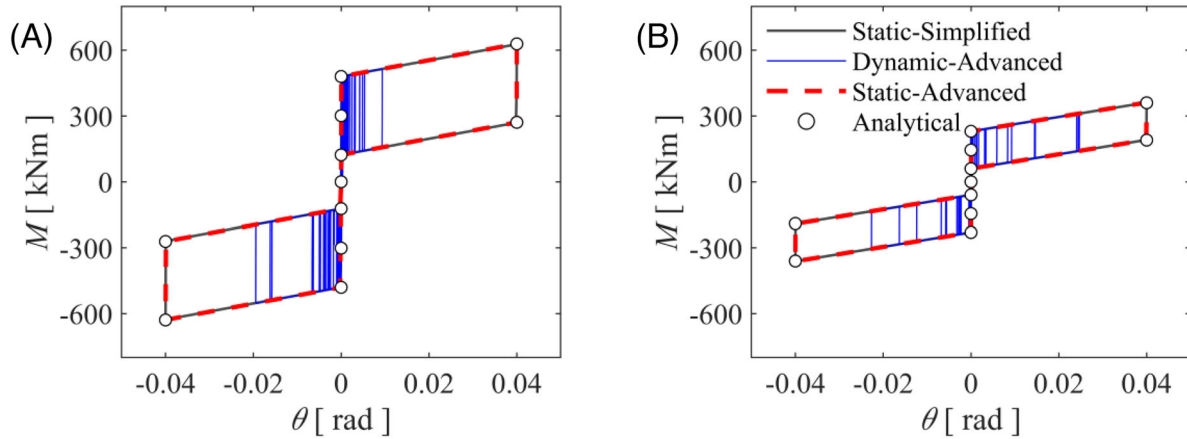


FIGURE 8 Moment–rotation behavior from analytical and OpenSees models of beam-to-column joints (BCJs) for: (A) story one external (EXT); and (B) story seven internal (INT)

both the advanced and the simplified modeling strategies. The comparison shows a perfect match for the cyclic responses, thus validating the simplified modeling approach.

In columns, during the seismic event, the axial force variation is significant due to both rocking behavior (i.e., PT bars elongation) and overturning moments. For this reason, for SCDF CBs the advanced model is used. Conversely, in beams, thanks to the disconnected and discontinuous slab, the axial force variation at the beam-to-column interface is only related to the rocking behavior and hence to the joint rotation. For this reason, and to reduce the model complexity, the simplified model is employed for SCDF BCJs. This model implicitly accounts for the PT force variation due to rocking as described in Section 2. Additionally, consisting of a simple rotational spring indirectly accounting for the effects of the rocking behavior, it has the advantage of being compatible with the model of the rigid slab. This strategy allows simplifying the modeling procedure and correctly capturing the behavior of the connection without detrimental effects on the results.

## 5 | PERFORMANCE-BASED ASSESSMENT

This section describes, analyzes, and critically compares the results obtained from the static push–pull (i.e., cyclic) analyses and IDAs for the investigated configurations. Static push–pull analyses are characterized by several simplifications (e.g., no considerations of the higher mode effects, no considerations of the dynamic response) and hence are used to provide a more straightforward and preliminary understanding of the seismic behavior of the structure. IDAs, considering a set of 30 ground motion records, are successively performed to obtain more comprehensive results, including considerations about the influence of the record-to-record variability.

### 5.1 | Static push–pull analyses

Non-linear static push–pull analyses are performed for all the considered configurations by applying a lateral force distribution compatible with the first mode of vibration and imposing a roof displacement equal to the mean value (among all ground motions), obtained by the non-linear time-history analyses for a seismic intensity corresponding to the ULS, as described in the following Subsection 5.2.

Figure 9 shows the relationship between the top story drift ratio ( $\theta_{top}$ ) and the base shear ( $V_b$ ) obtained from the push–pull static analyses. For illustration purposes, the comparison is reported for the three main (i.e., MRF, M-CB, M-BCJ) and five additional (i.e., C1, C12, C123, C1234, C12345) configurations selected to show the main trends. The following observations can be made:

- The M-BCJ shows a completely self-centering (i.e., flag-shape) behavior. Conversely, the MRF and M-CB show significant residual drifts coherently with previous research outcomes<sup>32</sup>.

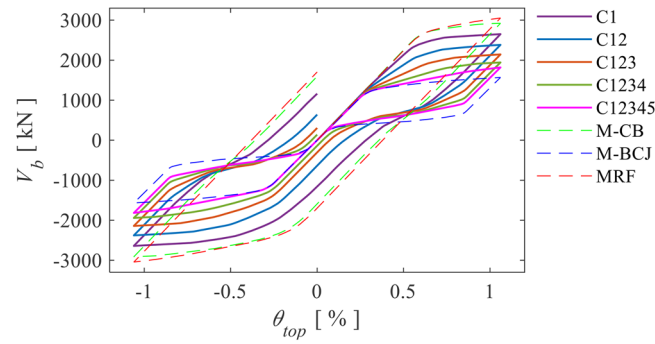


FIGURE 9 Push-pull results. Top story drift ratio ( $\theta_{top}$ ) versus base shear force ( $V_b$ ) for the configurations MRF, M-CB, M-BCJ, C1, C12, C123, C1234, and C12345

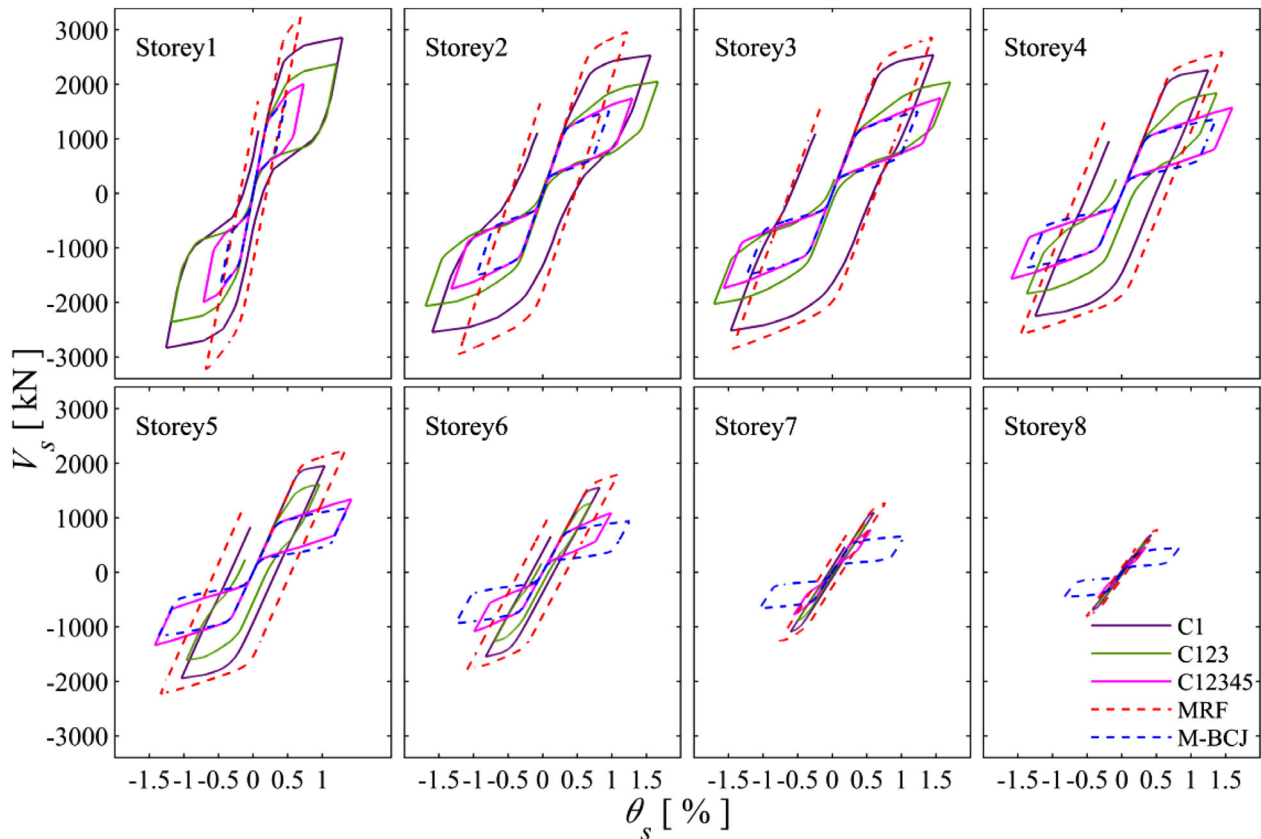
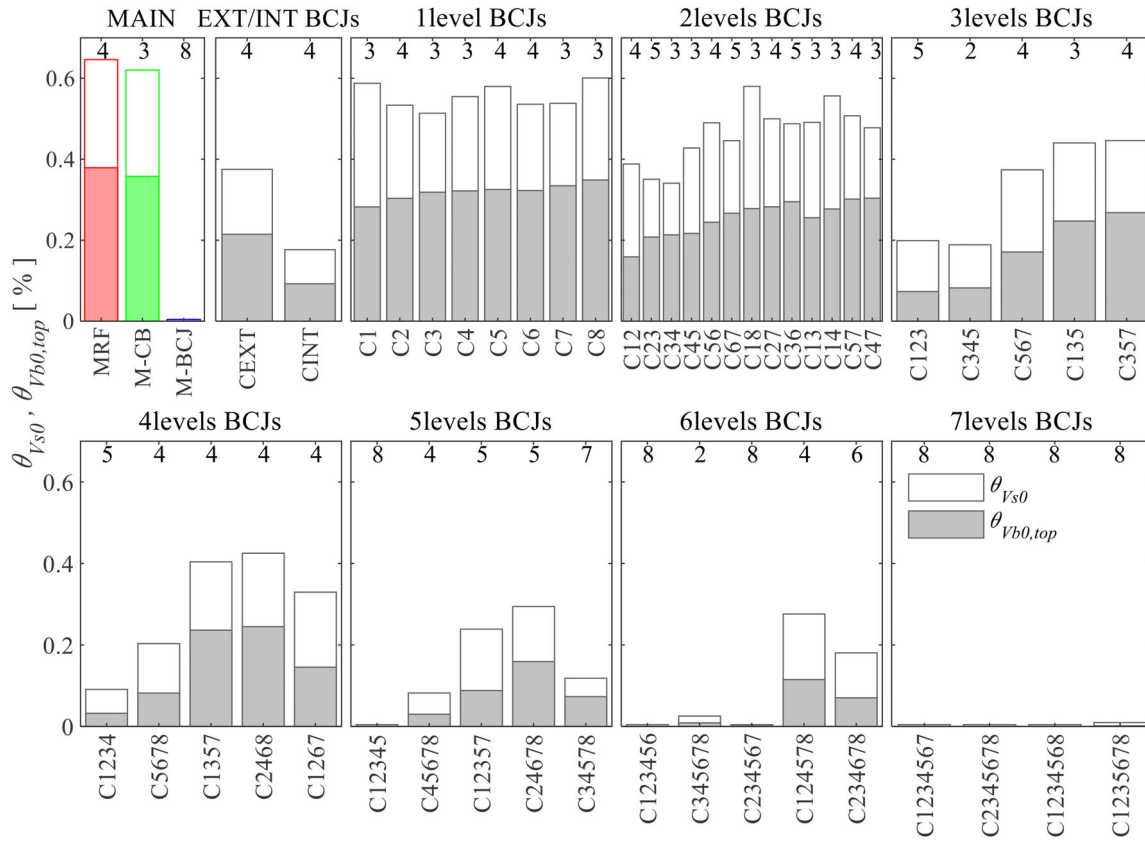


FIGURE 10 Push-pull results. Interstory drift ratio ( $\theta_s$ ) versus story shear ( $V_s$ ) for MRF, M-BCJ, C1, C123, and C12345

- The results of the other configurations show that by increasing the number of SCDF BCJs: (1) the self-centering capability of the structure is improved; (2) the maximum base shear of the push-pull curve is reduced due to the reduced bending moment capacity of the SCDF connections ( $M_2$ ) with respect to the yielding moment of the beams ( $M_y$ ) of the MRF.
- It is noteworthy that  $V_b$  reduction is related to the beams' overstrength in the MRF as its design is controlled by the deformability check at DLS.

Figure 10 shows the relationships between the interstory drift ratio ( $\theta_s$ ) and the story shear ( $V_s$ ) obtained from the push-pull analyses. For illustration purposes, the comparison is reported for the two main (i.e., MRF, M-BCJ) and three additional (i.e., C1, C123, C12345) configurations already presented in Figure 9. For the sake of clarity, the M-CB and the



**FIGURE 11** Push-pull results. Maximum interstory drift ratios corresponding to a zero story shear ( $\theta_{v_s0}$ ) and top drift ratios corresponding to a zero base shear force ( $\theta_{vb0,top}$ )

configurations C12, C1234 are not reported in the plot. The following observations can be made:

- The M-BCJ shows a completely self-centering (i.e., flag-shape) behavior at all stories. Conversely, the MRF shows significant inelastic deformations and the associated residual drifts at all stories.
- For C1 and C123, the self-centering behavior is evident in stories where the SCDF BCJs are applied while it progressively decreases for the other stories. C12345 shows the self-centering capability at all stories with a behavior similar to M-BCJ.
- It is noteworthy that, due to the reduced bending moment capacity and low post-elastic hardening of the SCDF connections, the results show higher  $\theta_s$  values at the stories where the SCDF devices are located. For example, this can be observed by (1) the comparison of C1 and MRF at story 1 where C1 shows significantly larger  $\theta_s$  values; or (2) the comparison of C12345 and M-BCJ at stories seven and eight where the M-BCJ shows significantly larger  $\theta_s$  values.
- It is clear that considering that the push-pull analyses are performed by imposing a constant value of the roof displacement, the use of SCDF devices at a limited number of stories results in larger  $\theta_s$  values at these stories. A more uniform distribution of SCDF devices results in more uniform  $\theta_s$  values at the different stories.
- The comparison of the C12345 and M-BCJ also shows that due to the (almost) elastic behavior of the C12345 at stories seven and eight, M-BCJ has no significant advantage in terms of the self-centering capability of the structure.

Figure 11 shows the maximum value (among all the stories) of the interstory drift ratios corresponding to a zero story shear ( $\theta_{v_s0}$ ) and the top drift ratios corresponding to a zero base shear force ( $\theta_{vb0,top}$ ), both measured at the end of the cycle of the push-pull curves (respectively in Figures 10 and 9). At the top of each bar is reported the number of the story where  $\theta_{v_s0}$  is achieved. The following observations can be made:

- The M-BCJ has negligible  $\theta_{v_s0}$  showing that applying SCDF CBs and SCDF BCJs at all stories ensures the self-centering behavior of the structure. Conversely, the M-CB has a  $\theta_{v_s0}$  marginally lower than the MRF, showing that SCDF CBs are ineffective in improving the seismic response of the building.
- All the configurations show a progressive reduction of  $\theta_{v_s0}$  while increasing the levels of SCDF BCJs.

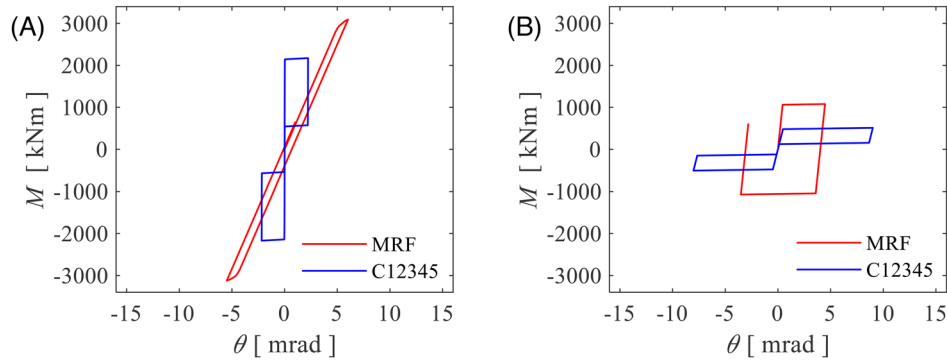


FIGURE 12 Push-pull results. Comparison of the moment-rotation behavior for: (a) column base internal (CB-INT); (b) beam-to-column joint internal (BCJ-INT) at story one

- Configurations with consecutive levels of SCDF BCJs applied at lower stories (e.g., C12, C23, C34, C123, C345, C1234, C112345, and C123456) show a more effective reduction of  $\theta_{V_{S0}}$  with respect to other configurations characterized by the same number of SCDF BCJs levels.
- $\theta_{V_{S0}}$  is generally observed at low stories except for the configurations with a high number of SCDF BCJs levels, where  $\theta_{V_{S0}}$  occurs at stories seven and eight.
- Although  $\theta_{V_{S0}}$  shows larger values of  $\theta_{V_{b0,top}}$ , they are characterized by the same trends. In fact,  $\theta_{V_{b0,top}}$  decreases progressively by increasing the number of SCDF BCJs levels and configuration with consecutive levels of SCDF BCJs applied at lower stories show a higher  $\theta_{V_{b0,top}}$  reduction.

Figure 12 shows the relationships in terms of moment-rotation behavior for an internal CB and an internal BCJ at story 1 for the MRF and C12345 obtained from the push-pull analyses. From the plots in Figure 12, and by monitoring the local responses of all configurations, the following observations can be made:

- All column's bottom and top sections remain elastic with the only exception for the CBs, which shows small inelastic deformations in the MRF (i.e., in the full-strength joints), while the flag-shape moment-rotation behavior is observed in the configurations equipped with the SCDF CBs (Figure 12A).
- The moment-rotation behavior of the BCJs shows an inelastic and hysteretic behavior in the MRF (i.e., plastic hinges) and the flag-shape moment-rotation behavior in the SCDF BCJs (Figure 12B).
- The moment-rotation behavior of the panel zones remains in the elastic range with no yielding at all stories.

From the just described results, the total dissipated energy ( $E_{tot}$ ) corresponding to a single cycle is calculated for each configuration as the sum of all CBs and BCJs moment-rotation integral. Figure 13A shows the  $E_{tot}$  of the main configurations (i.e., MRF, M-CB, M-BCJ). Negligible differences can be observed between the MRF and M-CB, showing that the CBs have a small contribution to  $E_{tot}$ . M-BCJ dissipates less energy than MRF due to the flag-shape behavior and the maximum moment reached by the SCDF BCJs, which is significantly smaller than the one reached in full-strength BCJs where the formation of the plastic hinge occurs. Overall  $E_{tot}$  decreases for increasing numbers of SCDF BCJs levels, and all the configurations have a value of  $E_{tot}$  between MRF and M-BCJ. Figure 13B shows the relation between the non-dimensional dissipated energy  $E$  (defined as  $E_{tot}/E_{tot,MRF}$ ) and the number of SCDF BCJs levels ( $n_{levels}$ ) by considering all configurations. The fitting of the results, based on an exponential regression, is shown in Figure 13B together with the mean values of the regression parameters ( $a$  and  $b$ ) defined with 95% confidence bounds, and the coefficient of determination ( $R^2$ ) calculated as a measure of the goodness of fit of the regression.

## 5.2 | Incremental dynamic analyses (IDAs)

IDAs<sup>38</sup> are performed to investigate the seismic performances of the 50 case-study frames accounting for the influence of the dynamic response and the influence of the uncertainty related to the earthquake input (i.e., record-to-record variability). The configurations are characterized by slightly different values of the fundamental vibration period due to the different stiffness of the connections ranging between 1.25 and 1.29 s where these two extreme values relate respectively



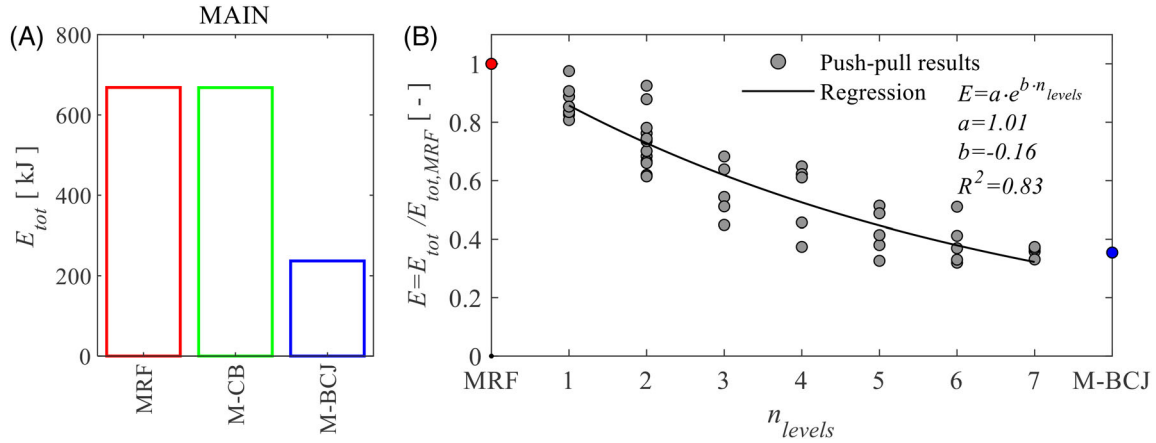


FIGURE 13 Push-pull results. (A) Total dissipated energy ( $E_{tot}$ ) for the main configurations (i.e., MRF, M-CB, M-BCJ); (B) non-dimensional dissipated energy ( $E$ ) versus the number of SCDF BCJs levels ( $n_{levels}$ ) and regression line

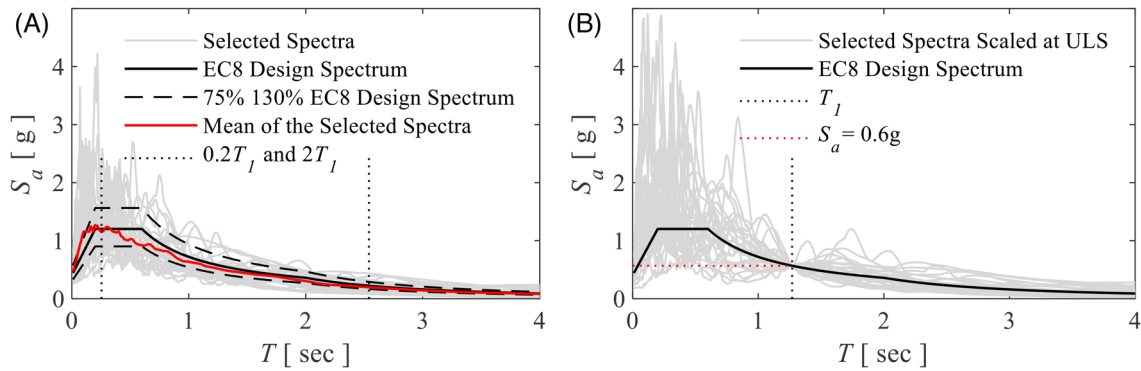


FIGURE 14 (A) Ground motions selection. (B) Ground motions records scaled at 0.6 g (i.e., intensity measure at ultimate limit state)

to the M-CB and M-BCJ. Therefore, it is useful to define  $T_{l,m} = 1.27$  s, representing the mean fundamental period among all configurations.

A suite of 30 ground motion records is selected from the SIMBAD database using REXEL<sup>39</sup>. The following input parameters are used: moment magnitude ( $M_w$ ) ranging from 6 to 7, epicentral distance  $R \leq 30$  km, and spectrum compatibility in the range of periods between  $0.2T_l$  and  $2T_l$ , where  $T_l$  is considered as  $T_{l,m}$ . The mean elastic spectrum of the records is kept between 75% and 130% of the corresponding Eurocode 8<sup>1</sup> elastic response spectrum considered for the design. The results of the ground motion selection are shown in Figure 14A. It is worth mentioning that a large number of zero acceleration points (i.e., 40 s) have been added at the end of each record to allow the free vibrations to stop and correctly capture the residual deformations. The just described set of ground motions is applied to all configurations. In order to allow the comparison of the IDAs' outcomes for the different configurations, the average spectral acceleration ( $avgSa$ ) (considering the range of periods from the stiffer to the most flexible structure) has been considered as IM. Given the small range of period variation, the  $avgSa$  is essentially equivalent to  $S_a(T_{l,m})$ . The IDAs are performed by scaling the ground motion records to increasing IM values with a constant step of 0.1 g until 1.0 g. The  $avgSa$  correspondent to a ULS seismic intensity is equal to 0.6 g, and Figure 14B shows the ground motion records scaled at it.

Global and story-level EDPs are monitored to investigate the effectiveness of the proposed configurations, including: (1) residual interstory drift ratios ( $\theta_{res}$ ); (2) peak interstory drift ratios ( $\theta_{peak}$ ); (3) peak story accelerations ( $a_{peak}$ ); and (4) residual top story drift ratios ( $\theta_{res,top}$ ). For the monitored story-level EDPs (i.e.,  $\theta_{res}$ ,  $\theta_{peak}$ ,  $a_{peak}$ ), the results reported in the following part refer to the maximum values among all stories.

The results of the IDAs are presented in two sections: (1) in Subsection 5.2.1 the stripe of the IDAs with an IM = 0.6 g (i.e., ULS) is taken into account, and the results (i.e.,  $\theta_{res}$ ,  $\theta_{peak}$ ,  $a_{peak}$ , and  $\theta_{res,top}$ ) are evaluated and compared for all the configurations; (2) in Subsection 5.2.2 all the results of IDA are considered and fragility curves based on  $\theta_{res}$  are derived for the most effective configurations.

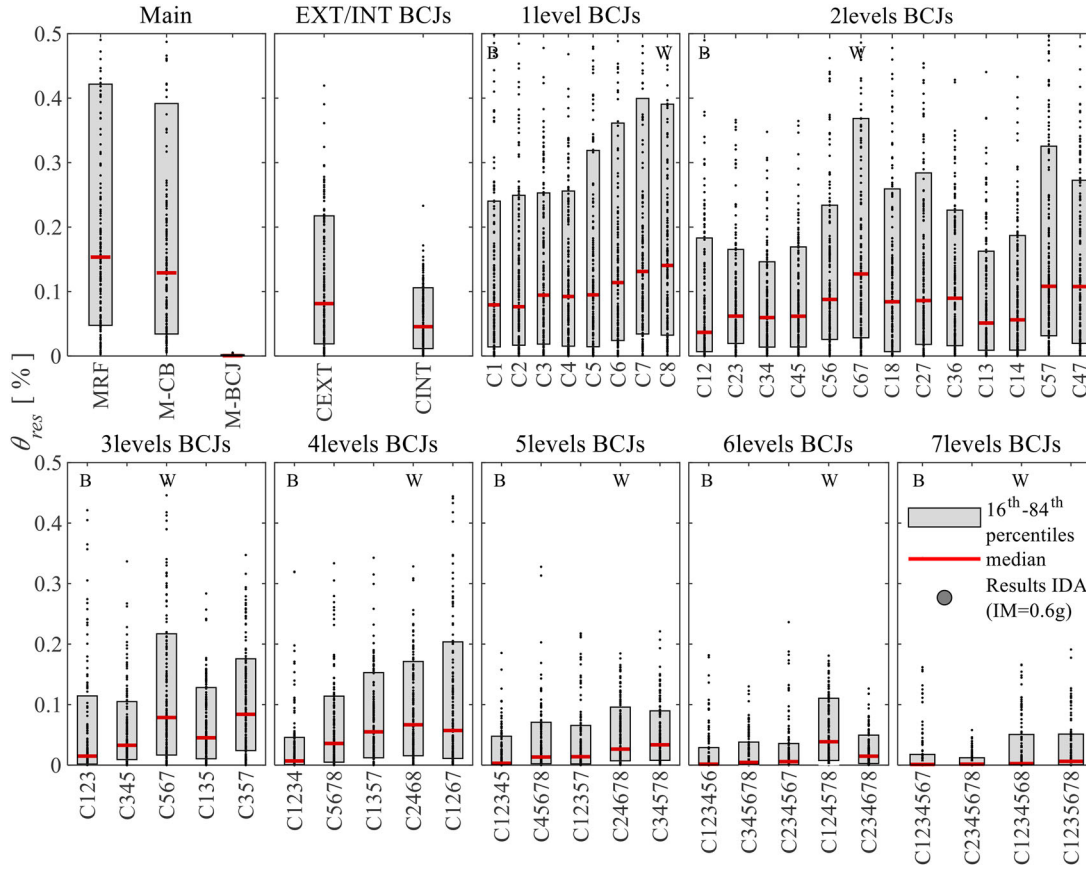


FIGURE 15 Stripe of the IDA with an IM = 0.6 g. Residual interstory drift ratios ( $\theta_{res}$ ) for all configurations

### 5.2.1 | Stripe of the IDAs with IM = 0.6 g

Figures 15 and 16 show the results of the stripe of the IDAs with an IM = 0.6 g (i.e., ULS) for all configurations, respectively, in terms of  $\theta_{res}$  at each story and  $\theta_{res,top}$ . For each configuration, the statistics of the results, including the median value (red lines) and the 16<sup>th</sup> and 84<sup>th</sup> percentiles (gray areas), are shown. For each number of SCDF BCJs levels, the “best” (B) and the “worst” (W) configurations are defined based on the median values of  $\theta_{res}$  and  $\theta_{res,top}$ , as indicated in the figures. For example, for one level of SCDF BCJs, C1 is defined as the “best” configuration while C8 as the “worst.”

It is worth reminding that the push–pull analyses (Figure 11) are performed for a roof displacement corresponding to the median value obtained by the stripe of the IDAs with IM = 0.6 g, hence allowing the comparison of the results. It is observed that  $\theta_{res}$  and  $\theta_{res,top}$  from the IDAs show respectively smaller values than  $\theta_{vs0}$  and  $\theta_{vb0,top}$  from the push–pull analyses highlighting that the dynamic effects in the IDAs promote the self-centering behavior of the structure. For example, for the MRF the results from the IDAs (Figure 15) provide a median value of  $\theta_{res}$  equal to 0.15%, which should be compared with the value of  $\theta_{vs0}$  equal to 0.65% obtained from the push–pull analysis (Figure 11). Similarly, for the MRF the median value of  $\theta_{res,top}$  equal to 0.13% (Figure 16) should be compared with the value of  $\theta_{vb0,top}$  equal to 0.38% (Figure 11). Among all configurations, the results from the IDAs show values of the order of 30% for both  $\theta_{res}$  and  $\theta_{res,top}$  with respect to the equivalent values obtained from the push–pull analyses. Nevertheless, the values of  $\theta_{res}$  and  $\theta_{res,top}$  obtained from IDAs (Figures 15 and 16) and the values of  $\theta_{vs0}$  and  $\theta_{vb0,top}$  obtained from push–pull analyses (Figure 11) show the same trends confirming that the use of consecutive levels of SCDF BCJs applied at lower stories represents a more effective strategy for residual drift reduction. It is noteworthy that the static push–pull analyses, despite being characterized by several simplifications (e.g., no considerations of the higher mode effects, no considerations of the dynamic response), allow the identification of the most effective configurations.

The results for  $\theta_{res}$  and  $\theta_{res,top}$  from the IDAs are further elaborated and synthesized. Figures 17A and 18A show the relationship between  $\theta_{res}$  and  $\theta_{res,top}$  and the number of SCDF BCJs levels ( $n_{levels}$ ). The figures show the fitting of the results, based on the exponential regression considering all configurations (Regression C-All). The gray areas show the 16<sup>th</sup> and

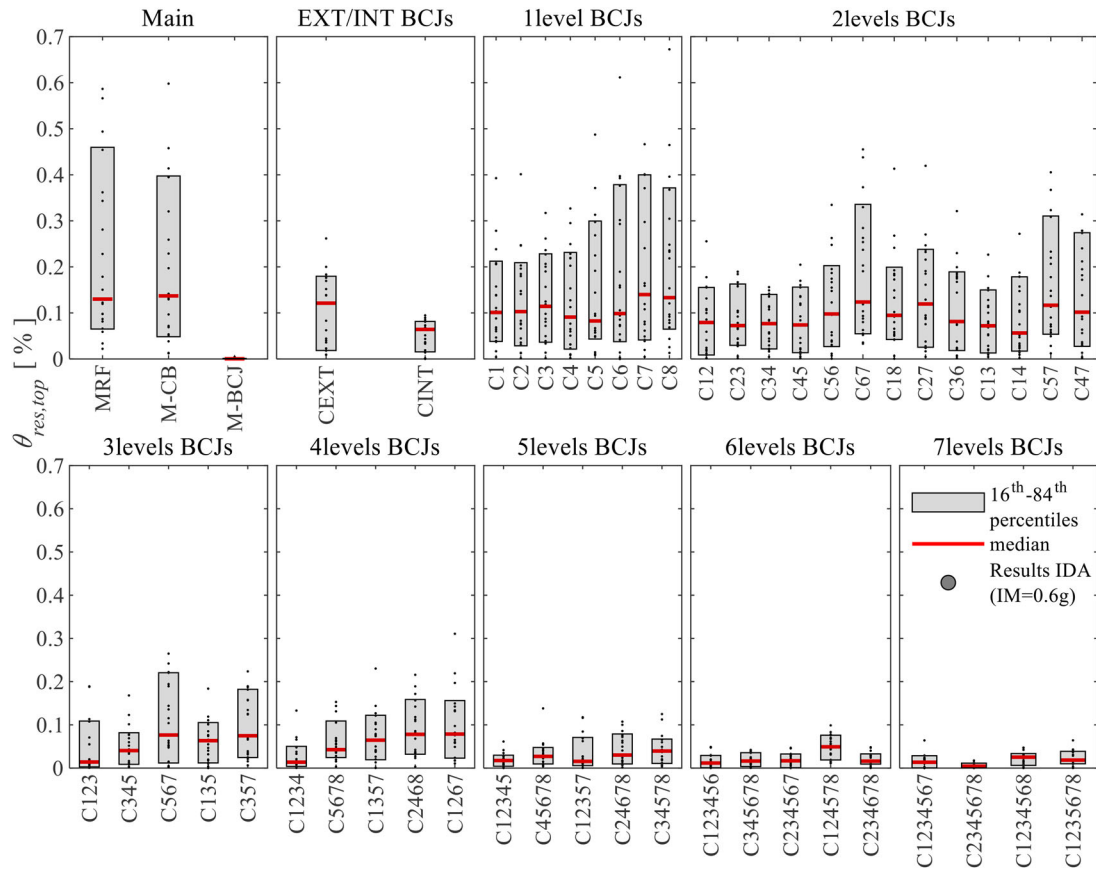


FIGURE 16 Stripe of the IDA with an IM = 0.6 g. Residual top story drift ratios ( $\theta_{res,top}$ ) for all configurations

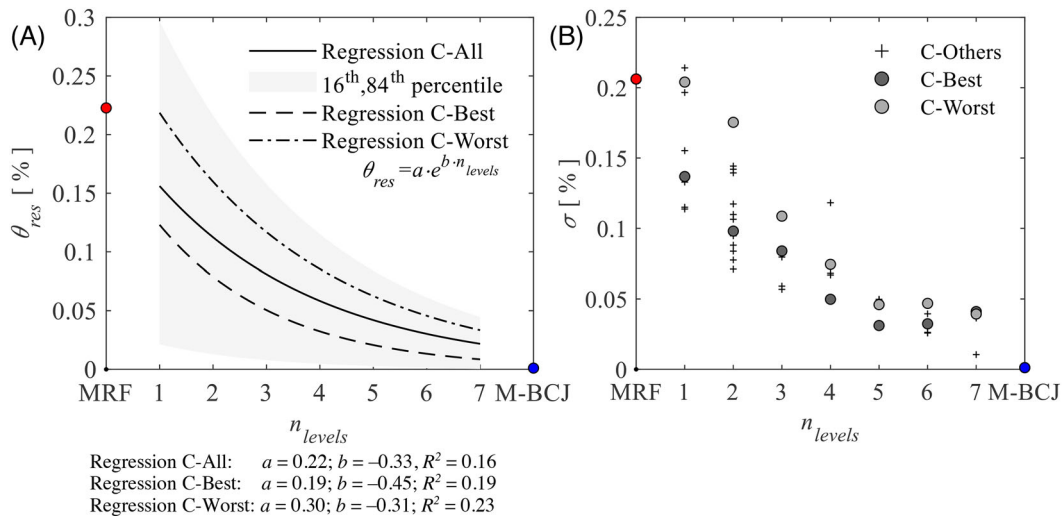


FIGURE 17 Stripe of the IDA with an IM = 0.6 g. (A) Regression lines for residual interstory drift ratios ( $\theta_{res}$ ). The red and blue dots represent the mean values of  $\theta_{res}$  for the MRF and M-BCJ; (B) standard deviations of residual interstory drift ratios ( $\theta_{res}$ )

84<sup>th</sup> percentile of the regression. Additionally, the regressions for the “best” (Regression C-Best) and “worst” (Regression C-Worst) configurations for each number of SCDF BCJs levels are shown. For the three regressions, the parameters ( $a$  and  $b$ ) are defined with 95% confidence bounds, and the coefficient of determination ( $R^2$ ) calculated as a measure of the goodness of fit of the regression. Overall, both  $\theta_{res}$  and  $\theta_{res,top}$  decrease for an increasing number of SCDF BCJs levels ( $n_{levels}$ ), for example, the inclusion of three levels of SCDF BCJs yields a decrease of  $\theta_{res}$  of 77% for the “best” configuration

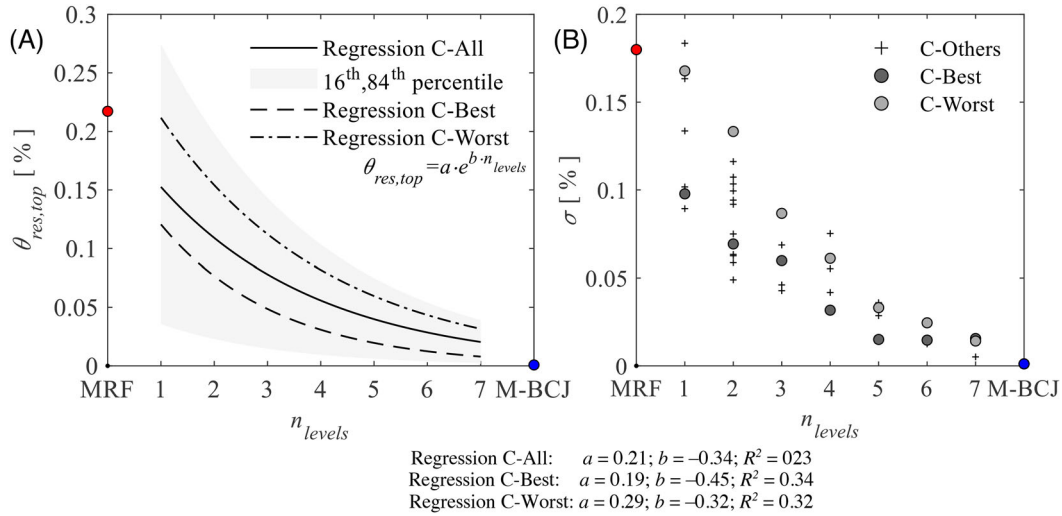


FIGURE 18 Stripe of the IDA with an IM = 0.6 g. (A) Regression lines for residual top story drift ratios ( $\theta_{res,top}$ ). The red and blue dots represent the mean values of  $\theta_{res,top}$  for the MRF and M-BCJ; (B) standard deviations of residual top story drift ratios ( $\theta_{res,top}$ )

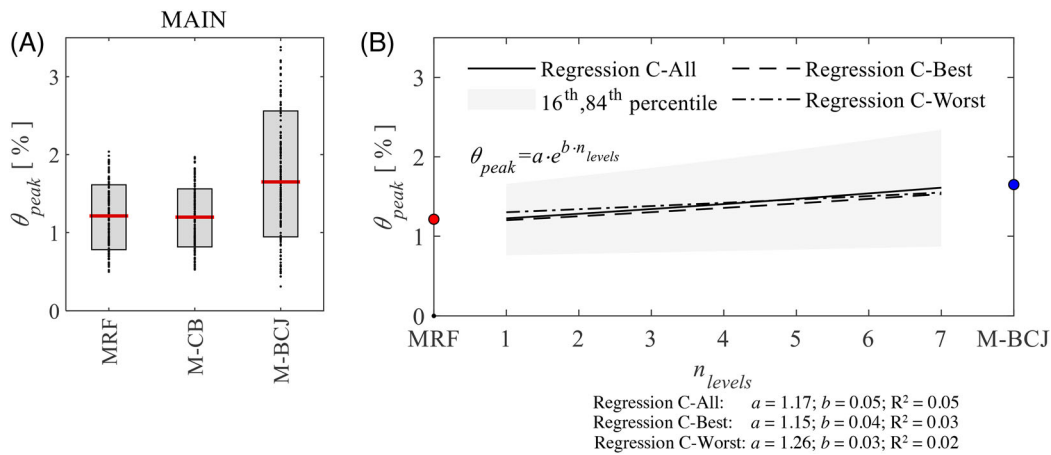


FIGURE 19 Stripe of the IDA with an IM = 0.6 g. Peak interstory drift ratios ( $\theta_{peak}$ ) for (a) the main configurations (i.e., MRF, M-CB, M-BCJ); (b) regression lines with respect to the number of SCDF BCJs levels ( $n_{levels}$ ). The red and blue dots represent the mean values of  $\theta_{peak}$  for the MRF and M-BCJ

and 48% for the “worst” with respect to the MRF. Figures 17B and 18B show the standard deviations ( $\sigma$ ) of the results of  $\theta_{res}$  and  $\theta_{res,top}$  for the “best” and “worst” configurations. It is noteworthy that the “best” configurations not only determine the lowest  $\theta_{res}$  values but also reduce the uncertainty of the results related to the record-to-record variability. Besides, it is also interesting to observe that, independently from the distribution of the devices, the inclusion of a larger number of SCDF BCJs levels leads to smaller values of  $\sigma$ .

Figures 19 and 20 show the results for  $\theta_{peak}$  and  $a_{peak}$ . These two parameters show less sensitivity to the number of SCDF BCJs levels ( $n_{levels}$ ). All the configurations have a value of  $\theta_{peak}$  and  $a_{peak}$  between the ones obtained for MRF and M-BCJs. Figures 19A and 20A show the results respectively for  $\theta_{peak}$  and  $a_{peak}$  for the main configurations (i.e., MRF, M-CB, M-BCJ). For each configuration, the statistics of the results are provided, showing the median values and the 16<sup>th</sup> and 84<sup>th</sup> percentiles. Figures 19B and 20B show the three regression lines for  $\theta_{peak}$  and  $a_{peak}$ , with respect to the number of SCDF BCJs levels. The following observations can be made:

- MRF and M-CB show almost identical  $\theta_{peak}$  values, while M-BCJ shows higher  $\theta_{peak}$  values with respect to MRF.

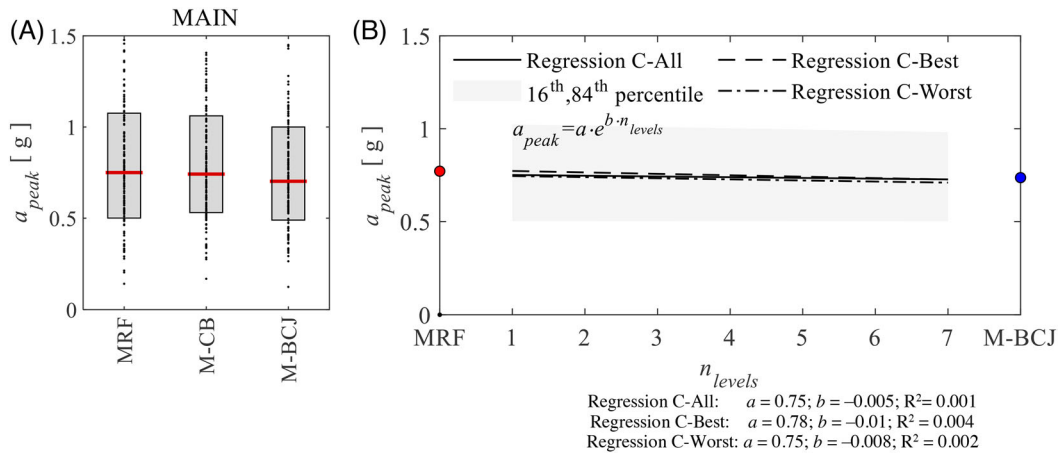


FIGURE 20 Stripe of the IDA with an  $IM = 0.6$  g. Peak acceleration ( $a_{peak}$ ) for (A) the main configurations (i.e., MRF, M-CB, M-BCJ); (B) regression lines with respect to the number of SCDF BCJs levels ( $n_{levels}$ ). The red and blue dots represent the mean values of  $a_{peak}$  for the MRF and M-BCJ

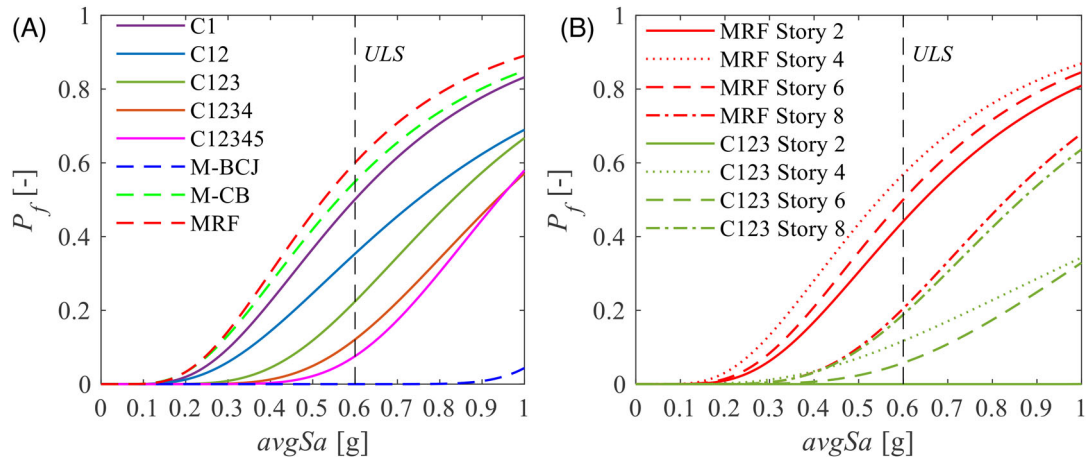


FIGURE 21 (A) System fragility curves: comparison between configurations MRF, M-CB, M-BCJ, C1, C12, C123, C1234; (B) story-level fragility curves: comparison between configurations MRF and C123 at stories two, four, six, and eight

- All the configurations have a value  $\theta_{peak}$  similar or higher than the one of the MRF, showing that the inclusion of SCDF connections leads to higher story displacements. This is related to the lower shear capacity and to the lower dissipation capacity of the systems for an increasing number of SCDF BCJs levels, as shown in Figure 13.
- All the regression lines are very similar, showing that, for a fixed number of SCDF BCJs levels, there is a small influence of their distribution.
- All the configurations have very similar values of  $a_{peak}$  with negligible differences. Also, in this case, all the regression lines are very similar with low variability of the results.

## 5.2.2 | Fragility curves

Fragility curves are derived based on residual interstory drifts (i.e.,  $\theta_{res}$ ) by considering the requirement of “no structural realignment” consisting in a capacity threshold of  $\theta_{res}$  equal to 0.2% as recommended by FEMA P58-1<sup>22</sup>. Fragility curves are numerically derived by the comparison of the samples of the demand for  $\theta_{res}$  with the capacity threshold and successively fitted by analytical lognormal curves through least-square minimization. Figure 21A shows system fragility curves (derived by assuming a series arrangement of the stories) for the three main configurations (i.e., MRF, M-CB, M-BCJ) and the five additional configurations (i.e., C1, C12, C123, C1234, C12345). The system fragility curves show that the results obtained

for the whole range of IM values are consistent with the ones obtained from the stripe of the IDAs with IM = 0.6 g (i.e., ULS). Figure 21B shows the story-level fragility curves derived for stories two, four, six, and eight of MRF and C123. It is possible to observe how the application of SCDF BCJs at one story leads to a  $P_f$  equal to zero for that story and to a decreasing  $P_f$  for all the others with respect to the MRF. For example, for C123, stories one, two, and three show a  $P_f$  equal to zero highlighting their self-centering capability. Only story two is reported in the figure, while stories one and three are not reported for the sake of clarity. In addition, it is possible to observe how the inclusion of the SCDF BCJs leads to a significant reduction of  $P_f$  in stories four, six, and eight with respect to the MRF.

The fragility curves confirm that the considerations obtained in the previous sections are valid for a wide range of IM values and confirm the design method's validity and robustness.

## 6 | CONCLUSIONS

The present study investigates the effective placement of a limited number of SCDF devices to be used within steel MRFs maximizing their beneficial effect on the seismic response. The used SCDF connection is based on a combination of FDs, which dissipate the seismic input energy, and a self-centering system, which, together with the gap opening mechanism, controls the self-centering behavior of the connection. A design procedure is defined to ensure the damage-free behavior of the structural element, the self-centering capability of the joint, and energy dissipation capacity. An eight-story steel MRF is designed, and 50 configurations with different locations of SCDF joints are considered. The three reference configurations consist of: (1) the conventional MRF with full-strength connections (indicated as MRF); (2) the equivalent MRF equipped with the SCDF CBs (indicated as M-CB); and (3) the equivalent MRF equipped with SCDF connections in both CBs and all BCJs (indicated as M-BCJ). Numerical models are developed in OpenSees. Non-linear static push-pull analyses are performed to monitor the local behavior of the structural elements and preliminary understand the overall behavior of the structure. Furthermore, incremental dynamic analyses (IDAs) are carried out considering a suite of 30 ground motion records taking into account the record-to-record variability. The stripe of the IDA with an intensity measure corresponding to the ultimate limit state is considered, and the results are evaluated and compared for all the configurations considering global and story-level engineering demand parameters. For some relevant configurations, fragility curves are derived based on residual deformations by considering the requirement of "no structural realignment" consisting of a capacity threshold of  $\theta_{res}$  equal to 0.2% as recommended by FEMA P58-1.

The analyses of the 50 configurations based on the eight-story case-study structure provide a general understanding of the effective placement of SCDF joints within steel MRFs. The quantitative results are limited to the considered case-study structure; however, several qualitative conclusions can be drawn and extended to other case studies.

As expected, conventional steel MRFs experience large residual drifts. Conversely, including SCDF connections at all CBs and BCJs ensures a completely self-centering (i.e., flag-shape) behavior leading to negligible residual interstory drift ratios ( $\theta_{res}$ ). However, applying SCDF BCJs at every story may not be the best solution since despite it allows having no residual drifts ( $\theta_{res}$ ), it leads to the highest structural complexity, limiting their practical application, and produces an increase of the peak interstory drift ratios ( $\theta_{peak}$ ) with respect to the MRF (e.g., for the investigated eight-story MRF it leads to an increase of  $\theta_{peak}$  of about 30%). To overcome this drawback, the present work focuses on the definition of effective placement for SCDF devices, maximizing their beneficial effect on the seismic response and controlling their impact on the overall structural complexity. The main outcomes can be summarized as follow.

- Significant residual drift ( $\theta_{res}$ ) reductions (with respect to the MRF) can be obtained including a limited number of SCDF BCJs levels, hence controlling both the structural complexity and the construction cost (e.g., for the investigated eight-story MRF the average value of  $\theta_{res}$  is reduced of 65% including three levels of SCDF BCJs only).
- The beneficial effect of including additional SCDF BCJs levels progressively decreases for higher numbers of SCDF BCJs levels (e.g., for the investigated eight-story MRF the average reduction of  $\theta_{res}$  obtained with respect to the MRF including one level of SCDF BCJs is about 30%, with two levels is about 50%, while with three levels is about 65% – Figure 17). This demonstrates that employing a large number of SCDF BCJs levels is not worthy in terms of improved seismic performance (i.e., residual interstorey drifts ( $\theta_{res}$ ) reduction).
- For a chosen number of SCDF BCJs levels, their placement significantly affects the seismic performance in terms of residual interstorey drifts ( $\theta_{res}$ ) reduction with respect to the MRF (e.g., for the investigated eight-story MRF with three levels of SCDF BCJs, the value of  $\theta_{res}$  obtained for the most effective placement is about 60% smaller than the one corresponding to the worst).

- The number and the placement of SCDF BCJs significantly affect not only the value of the residual interstorey drifts ( $\theta_{res}$ ) but also its uncertainties as a consequence of the record-to-record variability (e.g., for the investigated eight-story MRF, three levels of SCDF BCJs lead to a standard deviation of  $\theta_{res}$  that is about 50% smaller than the one observed using one level of SCDF BCJ; additionally within the MRF with three levels of SCDF BCJs, the standard deviation of  $\theta_{res}$  for the most effective placement is about 30% smaller than the one corresponding to the worst).
- Configurations with consecutive levels of SCDF BCJs at lower stories ensure a larger residual interstorey drift ( $\theta_{res}$ ) reduction compared to other configurations with the same number of SCDF BCJs levels.
- The maximum peak interstorey drift ratios ( $\theta_{peak}$ ) are less sensitive to the number of SCDF BCJs levels, while the maximum peak accelerations ( $a_{peak}$ ) have a negligible sensitivity.
- The abovementioned considerations are valid for a wide range of intensity measure values (e.g., for the investigated eight-story MRF this was confirmed by fragility curves).

The obtained conclusions provide general insights about how including a different number and placement of SCDF BCJs at different stories affects the seismic response of steel MRFs. However, in some cases, a few differences could exist. For example, in the case of steel MRFs with a larger number of stories, the effects of the higher vibration modes may lead to: (i) the application of SCDF BCJs at both lower and higher stories, (ii) the need of including a higher percentage of SCDF BCJs levels to satisfy the defined seismic performance in terms of residual interstorey drifts. In the case of steel MRFs with a larger number of bays, no significant differences are expected. However, in this case, it may be worth differentiating the behavior of the internal and the external BCJs hence considering that the joints belonging to the same story can be either conventional or SCDF. In the case of steel MRFs characterized by different seismic mass or seismic intensity, negligible differences are expected since these parameters are already considered in the design. Additional studies investigating a more comprehensive range of case studies and defining advanced tools are needed in order to further investigate and quantitatively discuss the aforementioned aspects.

## DATA AVAILABILITY STATEMENT

The data that support the findings of this study are available from the corresponding author upon reasonable request.

## ORCID

Ludovica Pieroni  <https://orcid.org/0000-0003-4776-2179>

Fabio Freddi  <https://orcid.org/0000-0003-2048-1166>

Massimo Latour  <https://orcid.org/0000-0001-9597-9503>

## REFERENCES

1. EN 1998-1. *Eurocode 8: Design of Structures for Earthquake Resistance – Part 1: General Rules, Seismic Actions, and Rules for Buildings*. European Committee for Standardization; 2004.
2. ANSI/AISC 341-16. *Seismic Provisions for Structural Steel Buildings*. American Institute of Steel Construction; 2016.
3. ASCE/SEI 7-16. *Minimum Design Loads and Associated Criteria for Buildings and Other Structures*. American Society of Civil Engineers; 2017.
4. Freddi F, Novelli V, Gentile R, et al. Observations from the 26th November 2019 Albania earthquake: the earthquake engineering field investigation team (EEFIT) mission. *Bull Earthq Eng*. 2021;19(5):2013–2044.
5. McCormick J, Aburano H, Ikenaga M & Nakashima M Permissible residual deformation levels for building structures considering both safety and human elements. Paper presented at: 14th World Conference of Earthquake Engineering; 2008; Beijing, China.
6. Freddi F, Galasso C, Cremen G, Dall'Asta A, Di Sarno L, Giaralis A, Gutiérrez-Urzúa F, Málaga-Chuquitaype C, Mitoulis S, Petrone C, Sextos A, Sousa L, Tarbali K, Tubaldi E, Wardman J, Woo G, et al. Innovations in earthquake risk reduction for resilience: recent advances and challenges. *Int J Disast Risk Reduct*. 2021;60:102267.
7. MacRae G, Clifton C, Bruneau M. New Zealand research applications of, and developments in, low damage technology for steel structures. *Key Eng Mater*. 2018;763:3–10.
8. Pampanin S. Reality-check and renewed challenges in Earthquake Engineering: implementing low-damage systems – from theory to practice. *Bull N Z Soc Earthq Eng*. 2012;45(4):137–160.
9. Soong TT, Spencer BF. Supplemental energy dissipation: state-of-the-art and state-of-the-practice. *Eng Struct*. 2002;24:243–259.
10. Seo CY, Karavasilis TL, Ricles JM, Sause R. Seismic performance and probabilistic collapse resistance assessment of steel moment resisting frames with fluid viscous dampers. *Earthq Eng Struct Dyn*. 2014;43(14):2135–2154.
11. Freddi F, Tubaldi E, Zona A, Dall'Asta A. Seismic performance of dual systems coupling moment-resisting frames and buckling-restrained braced frames. *Earthq Eng Struct Dyn*. 2021;50(2):329–353.

12. Freddi F, Ghosh J, Kotoky N, Raghunandan M. Device uncertainty propagation in low-ductility RC frames retrofitted with BRBs for seismic risk mitigation. *Earthq Eng Struct Dyn*. 2021. 50(9):2488–2509.
13. Mokhtari M, Naderpour H. Seismic resilience evaluation of base-isolated RC buildings using a loss-recovery approach. *Bull Earthq Eng*. 2020;18(10):5031–5061.
14. De Domenico D, Tubaldi E, Takewaki I, Karavasilis T, Dall'Asta A, Lavan O. Editorial: recent advances and applications of seismic isolation and energy dissipation devices. *Front Built Environ*. 2020;6:126.
15. Grigorian CE, Yang TS, Popov EP. Slotted bolted connection energy dissipators. *Earthq Spectra*. 1993;9(3):491–504.
16. Latour M, D'Aniello M, Zimbru M, Rizzano G, Piluso V, Landolfo R. Removable friction dampers for low-damage steel beam-to-column joints. *Soil Dyn Earthq Eng*. 2018;115:66–81.
17. Khoo HH, Clifton C, MacRae G, Zhou H, Ramhormozian S. Proposed design models for the asymmetric friction connection. *Earthq Eng Struct Dyn*. 2015;44(8):1309–1324.
18. Borzouie J, Macrae G, Chase JG, Rodgers GW. Cyclic performance of asymmetric friction connections with grade 10.9 bolts. *Bridg Struct Eng*. 2015;45(1):53–62.
19. Natri E, D'Aniello M, Zimbru M, et al. Seismic response of steel moment resisting frames equipped with friction beam-to-column joints. *Soil Dyn Earthq Eng*. 2019;119:144–157.
20. Latour M, Piluso V, Rizzano G. Experimental analysis of BCJs equipped with sprayed aluminium friction dampers. *J Struct Eng*. 2018;146:33–48.
21. Latour M, Piluso V, Rizzano G. Free from damage beam-to-column joints: testing and design of DST connections with friction pads. *Eng Struct*. 2015;85:219–233.
22. FEMA P58-1. *Seismic Performance Assessment of Buildings*. Volume 1 – Methodology. Applied Technology Council; 2012.
23. Ricles J, Sause R, Garlock M, Zhao C. Post-tensioned seismic-resistant connections for steel frames. *J Struct Eng*. 2001;127(2):113–121.
24. Kim H-J, Christopoulos C. Seismic design procedure and seismic response of post-tensioned self-centering steel frames. *Earthq Eng Struct Dyn*. 2009;38:355–376.
25. Vasdravellis G, Karavasilis TL, Uy B. Large-scale experimental validation of steel post-tensioned connections with web hourglass pins. *J Struct Eng*. 2013;139(6):1033–1042.
26. Dimopoulos C, Freddi F, Karavasilis TL, Vasdravellis G. Progressive collapse of self-centering moment resisting frames. *Eng Struct*. 2020;208:109923.
27. Freddi F, Dimopoulos CA, Karavasilis TL. Rocking damage-free steel CB with friction devices: design procedure and numerical evaluation. *Earthq Eng Struct Dyn*. 2017;46(14):2281–2300.
28. Freddi F, Dimopoulos CA, Karavasilis TL. Experimental evaluation of a rocking damage-free steel CB with friction devices. *J Struct Eng*. 2020;146(10):04020217.
29. Kamperidis VC, Karavasilis TL, Vasdravellis G. Self-centering steel CB with metallic energy dissipation devices. *J Constr Steel Res*. 2018;149:14–30.
30. Latour M, Rizzano G, Santiago A, da Silva LS. Experimental response of a low-yielding, self-centering, rocking CB joint with friction dampers. *Soil Dyn Earthq Eng*. 2019;116:580–592.
31. Elettore E, Freddi F, Latour M, Rizzano G. Design and analysis of a seismic resilient steel moment-resisting frame equipped with damage-free self-centring CBs. *J Constr Steel Res*. 2021;179:106543.
32. Elettore E, Lettieri A, Freddi F, Latour M, Rizzano G. Performance-based assessment of seismic-resilient steel moment resisting frames equipped with innovative column base connections. *Structures*. 2021;32:1646–1664.
33. Kim HJ, Christopoulos C. Seismic design procedure and seismic response of post-tensioned self-centering steel frames. *Earthq Eng Struct Dyn*. 2008;38(3):355–376.
34. Chou CC, Tsai KC, Yang WC. Self-centering steel connections with steel bars and a discontinuous composite slab. *Earthq Eng Struct Dyn*. 2009;38:403–422.
35. Tzimas AS, Dimopoulos AI, Karavasilis TL. EC8-based seismic design and assessment of self-centering post-tensioned steel frames with viscous dampers. *J Constr Steel Res*. 2015;105:60–73.
36. Mazzoni S, McKenna F, Scott MH, Fenves GL. *OpenSEES: Open System for Earthquake Engineering Simulation*. Pacific Earthquake Engineering Research Centre (PEER), University of California; 2009. <http://opensees.berkeley.edu>
37. Gutiérrez-Urzúa LF, Freddi F, Di Sarno L. Comparative analysis of code based approaches for the seismic assessment of existing steel moment resisting frames. *J Constr Steel Res*. 2021;181:106589.
38. Vamvatsikos D, Cornell CA. Incremental dynamic analysis. *Earthq Eng Struct Dyn*. 2002;31(3):491–514.
39. Iervolino I, Galasso C, Cosenza E. REXEL: computer-aided record selection for code-based seismic structural analysis. *Bull Earthq Eng*. 2010;8(2):339–362.
40. Bakalis K, Vamvatsikos D. Seismic fragility functions via nonlinear response history analysis. *J Struct Eng*. 2018;144(10):04018181.
41. Francavilla AB, Latour M, Piluso V, Rizzano G. Design criteria for beam-to-column connections equipped with friction devices. *J Constr Steel Res*. 2020;172:106240.
42. EN 1090-2. *Execution of Steel Structure and Aluminium Structure – Part 2: Technical Requirements for Steel Structures*. European Committee for Standardization; 2008.
43. EN 1993-1-8. *Eurocode 3: Design of Steel Structures – Part 1-8: Design of Joints*. European Committee for Standardization; 2005.



44. Lignos DG, Hikino T, Matsuoka Y, Nakashima M. Collapse assessment of steel moment frames based on E-Defense full-scale shake table collapse tests. *J Struct Eng*. 2013;139(1):120–132.
45. Ibarra LF, Medina RA, Krawinkler H. Hysteretic models that incorporate strength and stiffness deterioration. *Earthq Eng Struct Dyn*. 2005;34(12):1489–1511.
46. Lignos DG, Krawinkler H. Deterioration modeling of steel components in support of collapse prediction of steel moment frames under earthquake loading. *J Struct Eng*. 2011;137(11):1291–1302.
47. Charney FA, Downs WM. *Modeling procedures for panel zone deformations in moment-resisting frames*. Paper presented at: ESSC/AISC Workshop, Connections in Steel Structures; 2004; Amsterdam.
48. El Jisr H, Elkady A, Lignos DG. Hysteretic behaviour of moment-resisting frames considering slab restraint and framing action. *J Struct Eng*. 2020;146(8):04020145.
49. Zareian F, Medina RA. A practical method for proper modeling of structural damping in inelastic plane structural systems. *Comput Struct*. 2010;88(1-2):45–53.
50. Petrini L, Maggi C, Priestley N, Calvi M. Experimental verification of viscous damping modeling for inelastic time history analyses. *J Earthq Eng*. 2008;12(1):125–145.

**How to cite this article:** Pieroni L, Freddi F, Latour M. Effective placement of self-centering damage-free connections for seismic-resilient steel moment resisting frames. *Earthquake Engng Struct Dyn*. 2022; 1–25.  
<https://doi.org/10.1002/eqe.3615>